

## Structural Characterization of the *Mycobacterium tuberculosis* Biotin Biosynthesis Enzymes 7,8-Diaminopelargonic Acid Synthase and Dethiobiotin Synthetase<sup>†,‡</sup>

Sanghamitra Dey,<sup>#</sup> James M. Lane,<sup>||</sup> Richard E. Lee,<sup>⊥</sup> Eric J. Rubin,<sup>||</sup> and James C. Sacchettini<sup>\*§,¶</sup>

<sup>§</sup>Department of Biochemistry and Biophysics, Texas A&M University, College Station, Texas 77843, <sup>||</sup>Department of Immunology and Infectious Diseases, Harvard School of Public Health, Boston, Massachusetts 02115, <sup>⊥</sup>Chemical Biology and Therapeutics, St. Jude Children's Research Hospital, Memphis, Tennessee 38105, and <sup>#</sup>Department of Biochemistry and Biophysics, Texas A&M University, College Station, TX 77843. <sup>¶</sup>Current address: University of California, San Diego, La Jolla, California 92093.

Received December 7, 2009; Revised Manuscript Received March 12, 2010

**ABSTRACT:** *Mycobacterium tuberculosis* (*Mtb*) depends on biotin synthesis for survival during infection. In the absence of biotin, disruption of the biotin biosynthesis pathway results in cell death rather than growth arrest, an unusual phenotype for an *Mtb* auxotroph. Humans lack the enzymes for biotin production, making the proteins of this essential *Mtb* pathway promising drug targets. To this end, we have determined the crystal structures of the second and third enzymes of the *Mtb* biotin biosynthetic pathway, 7,8-diaminopelargonic acid synthase (DAPAS) and dethiobiotin synthetase (DTBS), at respective resolutions of 2.2 and 1.85 Å. Superimposition of the DAPAS structures bound either to the SAM analogue sinefungin or to 7-keto-8-aminopelargonic acid (KAPA) allowed us to map the putative binding site for the substrates and to propose a mechanism by which the enzyme accommodates their disparate structures. Comparison of the DTBS structures bound to the substrate 7,8-diaminopelargonic acid (DAPA) or to ADP and the product dethiobiotin (DTB) permitted derivation of an enzyme mechanism. There are significant differences between the *Mtb* enzymes and those of other organisms; the *Bacillus subtilis* DAPAS, presented here at a high resolution of 2.2 Å, has active site variations and the *Escherichia coli* and *Helicobacter pylori* DTBS have alterations in their overall folds. We have begun to exploit the unique characteristics of the *Mtb* structures to design specific inhibitors against the biotin biosynthesis pathway in *Mtb*.

Biotin is a cofactor for essential enzymes that function in carboxylation, decarboxylation, and transcarboxylation reactions found in many processes such as fatty acid biosynthesis, gluconeogenesis, and amino acid metabolism (1). Whereas plants and bacteria, including *Mtb*,<sup>1</sup> have enzymes for production of this cofactor, mammals do not, instead obtaining biotin through diet and the action of gut bacteria. This makes the *Mtb* biotin synthetic pathway an attractive drug target.

*Mtb* relies on biotin utilizing pathways, especially fatty acid biosynthesis, during latency (2), and multiple lines of evidence suggest that biotin production is essential for mycobacterial survival *in vitro* and *in vivo*. In the model organism *Mycobacterium smegmatis*, the *bioA* gene, which encodes the second enzyme in the biosynthetic pathway 7,8-diaminopelargonic acid synthase (DAPAS), is required for optimal stationary phase growth in

rich, biotin-replete medium (3). This suggests that *de novo* biotin biosynthesis is required during the stationary phase and that mycobacteria in this phase are unable to acquire biotin from the medium. In *Mtb* expression of *bioD*, the gene encoding dethiobiotin synthase (DTBS), the third enzyme in the biosynthetic pathway, is upregulated after 96 h of nutrient starvation (4), a condition thought to mimic bacterial persistence *in vivo* (2). Finally, disruption of the *Mtb* biotin biosynthesis machinery by transposon mutagenesis results in rapid clearance of the mutants in the early stages of infection (5). This is unsurprising, as biotin auxotrophy has been linked to the attenuation of virulence in other bacterial pathogens (6).

The *Mtb* H37Rv genome encodes all four enzymes needed to convert pimeloyl-CoA to biotin (Figure 1) (7), although the source of pimeloyl-CoA in *Mtb* has not yet been identified. KAPA synthase (BioF: Rv1569), a pyridoxal 5'-phosphate (PLP) dependent enzyme, catalyzes the first step of biotin biosynthesis, the decarboxylative condensation of pimeloyl-CoA with L-alanine to produce 7-keto-8-aminopelargonic acid (KAPA). In the second step of the pathway, the PLP-dependent DAPA synthase (BioA: Rv1568) uses S-adenosylmethionine (SAM) to transaminate KAPA into 7,8-diaminopelargonic acid (DAPA). Dethiobiotin synthetase (BioD: Rv1570) carboxylates DAPA to form the ureido ring of dethiobiotin (DTB) in the ATP- and magnesium-dependent third step of the pathway. Finally, biotin synthase (BioB: Rv1589), an iron-sulfur cluster enzyme, converts DTB into biotin, generating a free radical via SAM in the fourth and final step of biotin production.

There have been initial biochemical characterizations of the biotin biosynthetic enzymes in microbes such as *Bacillus sphaericus* (8)

<sup>†</sup>This work was supported by National Institutes of Health Grant PO1AIO68135 and by funds from the Robert A. Welch Foundation for J.C.S. and by the American Lebanese Syrian Associated Charities (ALSAC) for R.E.L.

<sup>‡</sup>The coordinates for these structures are available from the Protein Data Bank (ID codes 3BV0, 3LV2, 3DRD, 3DOD, 3DU4, 3FGN, 3FMF, 3FMI, and 3FPA).

\*To whom correspondence should be addressed: e-mail, sacchett@tamu.edu; phone, 979-862-7636; fax, 979-862-7638.

Abbreviations: *Mtb*, *Mycobacterium tuberculosis*; DAPAS, 7,8-diaminopelargonic acid synthase; DTBS, dethiobiotin synthetase; PLP, pyridoxal 5'-phosphate; KAPA, 7-keto-8-aminopelargonic acid; SAM, S-adenosylmethionine; DAPA, 7,8-diaminopelargonic acid; DTB, dethiobiotin; PMP, pyridoxamine phosphate; AMPSO, N-(1,1-dimethyl-2-hydroxyethyl)-3-amino-2-hydroxypropanesulfonic acid; SAH, S-adenosylhomocysteine; ATP, adenosine triphosphate; ADP, adenosine diphosphate.

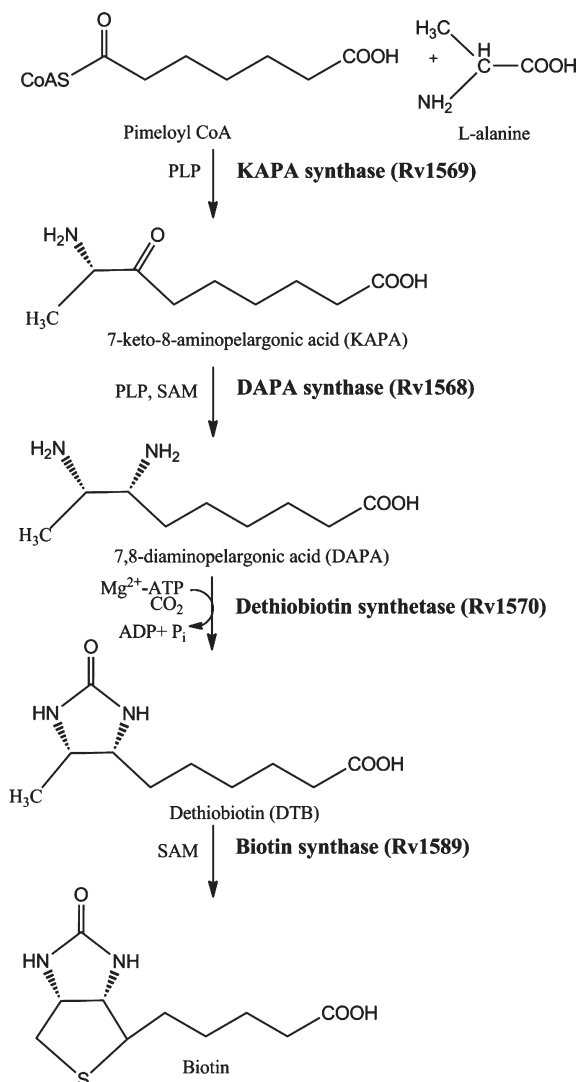


FIGURE 1: The *Mtb* biotin synthetic pathway showing the four enzymes required to convert pimeloyl-CoA and alanine to biotin.

and *Bacillus subtilis* (9), the lower eukaryote *Saccharomyces cerevisiae* (10), and in the plant *Arabidopsis thaliana* (11), but the pathway has been most thoroughly studied in *Escherichia coli* (12–20). Indeed, the *E. coli* enzymes' crystal structures have served as the basis for several studies that attempted to define inhibitors of the plant biotin pathway for herbicide development (21–23).

Here we present the structural characterization of two *Mtb* biotin biosynthetic enzymes, DAPAS and DTBS, and our subsequent efforts to develop inhibitors of this *Mtb* pathway. Although there are two known natural inhibitors with strong whole cell activity, amiclennomycin (MIC = 3.1  $\mu\text{g}/\text{mL}$ ) (24) and acidomycin (MIC = 0.0625–0.125  $\mu\text{g}/\text{mL}$ ) (25), both amiclennomycin (26) and acidomycin (27) were demonstrated to be inactive in a mouse model of tuberculosis (Figure 2). Previous transposon mutagenesis work indicates that *Mtb* is not able to scavenge biotin from the host, and the failure of acidomycin to work *in vivo* appears to be the result of limited bioavailability (27). We show here that the biotin biosynthesis pathway is required for *Mtb* survival *in vitro*, a surprising finding for an *Mtb* auxotroph.

The *Mtb* DAPAS and DTBS structures also shed light on the enzymes' kinetics and mechanisms of action. With a 48% sequence identity, the efficiency of *Mtb* DAPAS is similar to its

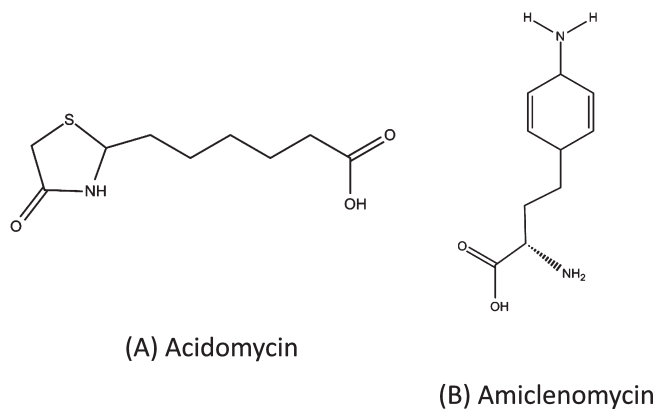


FIGURE 2: The chemical structures of the known inhibitors of the biotin biosynthetic pathway: (A) acidomycin; (B) amiclennomycin.

*E. coli* counterpart ( $k_{\text{cat}}$  for *Mtb* and *E. coli* DAPAS are  $1 \pm 0.2/\text{min}$  and  $0.78/\text{min}$ , respectively) (14, 28); however, the  $K_m$  value for its amino donor SAM is higher ( $750 \pm 200 \mu\text{M}$  in *Mtb* compared to  $150 \mu\text{M}$  in *E. coli*) (14, 28). We present evidence that differences between the active site architecture of the *Mtb* and *E. coli* DAPAS enzymes may account for the small but noticeable differences in the kinetic behavior between them. Structures of substrate-bound *Mtb* DAPAS and of its *B. subtilis* homologue also provide insight into the mode of and variability in dual substrate recognition at the active site of this aminotransferase. Finally, comparison of the apo and substrate-bound forms of *Mtb* DTBS delineates the binding mode of the substrate as well as the mechanism of enzyme catalysis, while comparison of DTBS structures from multiple species highlights the substantial natural variability in structural folds.

## MATERIALS AND METHODS

**Growth of *Mycobacterium tuberculosis*.** *Mtb* H37Rv  $\Delta\text{bioF}$  was maintained in Middlebrook 7H9 medium with glycerol and Tween 80 or in Sauton's medium supplemented with  $50 \mu\text{M}$  biotin (5).

**Cloning, Protein Expression, and Purification.** The *bioA* (Rv1568) and *bioD* (Rv1570) genes from *Mtb* H37Rv genomic DNA were amplified and cloned into the pET28b vector (Novagen) with the TEV site using the *NdeI* and *HindIII* sites. The Y25A mutant of *Mtb* DAPAS was constructed using the QuikChange site-directed mutagenesis kit (Stratagene) and cloned into the same modified pET28b vector. The *NdeI* site containing the ATG start codon and the stop codon precedes the *HindIII* site. Both clones were then transformed into the *E. coli* overexpression host BL21(DE3). The transformed cell culture was grown in LB medium with kanamycin ( $50 \mu\text{g}/\text{mL}$ ) at  $37^\circ\text{C}$  until the  $A_{600}$  reached 0.8 and then was induced with 0.5 mM IPTG at  $25^\circ\text{C}$  and grown overnight. There was no overexpression seen at temperatures lower than  $25^\circ\text{C}$ . The cells were harvested by centrifuging at 4000 rpm for 30 min and resuspended in 50 mM Tris buffer (pH 7.5), 500 mM NaCl, 1 mM PMSF, DNase ( $20 \mu\text{g}/\text{mL}$ ), and  $100 \mu\text{M}$  PLP (for DAPAS only). The cells were lysed using a French press at 1200 psi, and cell debris was removed by centrifuging the cell lysate at 15000 rpm for 1 h. The filtered supernatant was then loaded on a pre-equilibrated (50 mM Tris buffer (pH 7.5), 500 mM NaCl) Hitrap nickel column (GE Healthcare) and washed. Protein elution with an imidazole gradient (50–400 mM) followed. The fractions containing pure protein were pooled and dialyzed overnight against

a buffer containing 25 mM Tris buffer (pH 7.5), 50 mM NaCl, 1 mM EDTA, and 1 mM DTT. The purity of the proteins was judged from a 4–12% gradient SDS–PAGE gel.

The *B. subtilis bioA* gene was PCR-amplified from *B. subtilis* 168 genomic DNA (Bacillus Genetic Stock Centre, Ohio State University) and further cloned and purified in the same way as *Mtb* DAPAS and DTBS.

**Spectroscopic Studies of *Mtb* DAPAS and DTBS.** Absorbance spectra for wild-type *Mtb* DAPAS with 1 mM SAM, sinefungin, or SAH and for the Y25A mutant DAPAS with SAM and DAPA were measured on the Cary 50 spectrophotometer (Varian) in the range of 300–600 nm. Fluorescence emission scans for *Mtb* DAPAS with 1 mM sinefungin and SAH were followed in the range of 300–450 nm on the LS 55 luminescence spectrometer (Perkin-Elmer Instruments) with constant stirring. All experiments were carried out at room temperature. The buffer used was 50 mM AMPPO (pH 8.5), 150 mM NaCl, 10% glycerol, 4 mM  $\beta$ -mercaptoethanol, and 100  $\mu$ M PLP.

Coupled assays for wild-type and D47A mutant *Mtb* DTBS with pyruvate kinase/lactate dehydrogenase (29) were carried out to determine the kinetic parameters of ATP and DAPA by keeping the other substrate at a saturating concentration of 3 mM and 50  $\mu$ M, respectively. The buffer used for the 500  $\mu$ L assay contained 50 mM Tris (pH 7.5), 150 mM NaCl, 10 mM NaHCO<sub>3</sub>, and 5 mM MgCl<sub>2</sub>. ADP formation in the DTBS reaction was measured by monitoring the decrease in NADH absorbance at 340 nm. These assays were carried out using a Cary 100 spectrophotometer. DAPAS and DTBS concentrations were calculated from their absorbance at 280 nm using extinction coefficients ( $\epsilon = 64490 \text{ mM}^{-1} \text{ cm}^{-1}$  and  $\epsilon = 12840 \text{ mM}^{-1} \text{ cm}^{-1}$ , respectively) (30).

**Crystallization and Data Collection.** The crystal trials for *Mtb* and *B. subtilis* DAPAS and *Mtb* DTBS were carried out at 18 °C using Crystal Screens I and II, Index, Membfac, and PEG/Ion screens (Hampton Research) and the Wizard I, II, and III screens (Emerald Biosystems). Initial hits were obtained using robotic screening with a 1:1 ratio of protein to precipitant on 96-well Intelli-Plates (Hampton Research).

Yellow crystals for *Mtb* DAPAS appeared after heavy precipitation under different conditions with PEG 8000 as the common precipitant. These crystals were obtained from a DAPAS protein with a random mutation at position 315 (H315R). A high-resolution data set for the *Mtb* DAPAS crystal obtained in 10% PEG 8000, 0.1 M Tris buffer (pH 7.0), and 0.1 M MgCl<sub>2</sub> (Wizard II no. 43) was collected at Cu wavelength using the home source to a resolution of 2.2 Å. The data set for sinefungin-bound DAPAS was obtained by soaking the crystal in 10 mM sinefungin for 45 min. The crystal was obtained in Hampton Research's Index screen no. 46 (20% PEGMME 5000, 0.1 M Bis-Tris buffer (pH 7.5)). Soaking the crystals for a longer amount of time or using a higher concentration of sinefungin resulted in significant deterioration of diffraction or no diffraction at all. The data set was collected in-house on a Rigaku R-axis IV++ detector at a resolution of 2.2 Å.

Crystals for *B. subtilis* DAPAS were obtained in a 4  $\mu$ L hanging drop with a 1:1 ratio of protein (10 mg/mL) to precipitant in 20% PEG 3350 and 0.2 M sodium thiocyanate (PEG/ion screen no. 13; Hampton Research). The quality of the crystal greatly improved with the addition of 5% xylitol from the additive screen (no. 56 of Hampton Research). The PLP-bound structure and PLP- and KAPA-bound structures were obtained by cocrystallization of the DAPAS protein with 1 mM PLP or

1 mM PLP and 5 mM KAPA, respectively, in hanging drop plates. Simple soaking of DAPAS crystals in drops containing PLP or KAPA resulted in no diffraction.

The native *Mtb* DTBS protein crystals were obtained in 1 M sodium citrate and 0.1 M imidazole (pH 7.5) (Wizard I no. 36). Molecular replacement using the *E. coli* DTBS structure (PDB code: 1BYI) (31) as a template was not successful. Thus native DTBS crystals were soaked in 50 mM samarium chloride for 1 h, and a data set at 2.6 Å resolution was collected using a Rigaku Raxis IV++ detector at Cu wavelength (1.54 Å). The DAPA-, KAPA-, and DTB-ADP-complexed DTBS structures were obtained by soaking the native crystals overnight in 10 mM DAPA, 10 mM KAPA, or 10 mM DTB, 10 mM ADP, and 10 mM MgCl<sub>2</sub>, respectively. The DAPA- and KAPA-bound data sets were collected from the crystals obtained in the same condition as the native. The DTB-ADP complexed structure was obtained from crystals in 0.4 M sodium phosphate/1.6 M potassium phosphate, 0.1 M imidazole (pH 8.0), and 0.2 M NaCl.

All diffraction data were collected at 120 K using DAPAS and DTBS crystals cryoprotected in paratone oil.

**Data Processing, Structure Determination, and Refinement.** *Mtb* and *B. subtilis* DAPAS and *Mtb* DTBS data were reduced and scaled using the HKL 2000 suite (32), d\*trek (33), mosflm (34), and SCALA (35).

The structure of PLP-bound *Mtb* DAPAS was determined by molecular replacement using PHASER (36) to provide clear solutions. The *E. coli* DAPAS monomer (PDB code: 1QJ5) (15) was used as the model (LLG = 1437.551). The structure of sinefungin-bound DAPAS was solved by molecular replacement using the PLP-bound *Mtb* DAPAS as the model (LLG = 4189.75). Phasing of the *B. subtilis* DAPAS data set was also achieved by the molecular replacement method using the coordinates of *Mtb* DAPAS chain A (LLG = 279) as the search model for PHASER. The LLG was 243 using the *E. coli* DAPAS monomer (PDB code: 1QJ5).

For determination of the *Mtb* DTBS structure, four sites for samarium (Sm) were found as the anomalous difference Patterson peaks using SHELXD (37). After refining these Sm sites and performing initial phasing with AutoSHARP (38), we obtained a density-modified map by solvent flattening using DM. The phases were further extended to a high-resolution native data set of 1.85 Å for the DTBS apo structure. DAPA-, KAPA-, and DTB-, ADP-, and P<sub>i</sub>-complexed structures were obtained by refining the DTBS apo structure against these data, which have similar unit cell dimensions.

Iterative rounds of model building were performed using Xtalview (39) and Coot (40) with the Shake&wARP (41) unbiased electron density maps. Initially, one round of simulated annealing at 4000 K using CNS (42) was performed to improve the geometry of the models and to remove bias from the model. Water molecules were then added to the models after the *R*-factor and *R*<sub>free</sub> were below 30% and inspected manually after refinement. The quality of the models was validated by Ramachandran plot using the program PROCHECK (43).

## RESULTS AND DISCUSSION

**Biotin Synthesis Is Required for Bacterial Survival *In Vitro*.** We previously constructed an *Mtb* strain with an in-frame deletion of *bioF*, the gene that encodes KAPA synthase. This mutant is unable to establish an infection in mice and is rapidly cleared (5). We found that *in vitro* growth of the *bioF* strain is

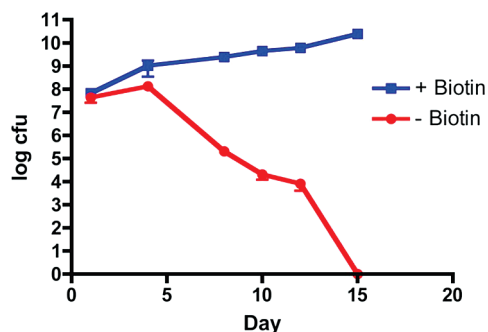


FIGURE 3: Survival of the *bioF* *Mtb* mutant is dependent on biotin. A  $\Delta$ *bioF* *Mtb* strain was grown in Sauton's medium in the presence or absence of 50  $\mu$ M biotin. Surviving colonies were quantified by measuring growth on biotin-containing Middlebrook 7H10 medium at the indicated time points. Data represent mean  $\pm$  SEM of triplicate samples. The threshold of detection is 100 colonies.

completely dependent on the addition of exogenous biotin to the culture medium (Figure 3). Unexpectedly, there is no measurable survival of the mutant following 2 weeks of biotin depletion even after replating on medium supplemented with biotin (Figure 3). This irreversible cell death phenotype is unusual as *Mtb* auxotrophs typically do not die when starved for their given nutrient *in vitro* but instead enter a nonreplicative phase that can be reversed by addition of the nutrient (44, 45). Biotin appears to be different; mycobacteria may be unable to sense biotin depletion and grow in the absence of essential metabolites whose synthesis is biotin-dependent. In this regard, the *Mtb bioF* mutant is reminiscent of the *M. smegmatis dapA* strain, which lyses because it continues to grow despite being unable to synthesize a normal cell wall (46). Alternatively, biotin may aid in defense against a continual, unknown stress.

Analysis of whole genome screening data suggests that it is unlikely that *bioF* has a unique role in mycobacterial physiology and virulence. Mutations in two (*bioA* and *bioB*) of the three other predicted biotin synthesis genes lead to decreased *in vivo* growth (5). Although the degree of attenuation is not as profound as that produced by the *bioF* mutation, this type of screen is not perfectly quantitative. Thus, biotin synthesis at any step is likely essential for *Mtb* growth during infection and for survival in culture.

**Biochemical Characterization of *Mtb* DAPAS.** The PLP-dependent enzyme DAPAS transfers the amino group from SAM to KAPA to form DAPA. Aminotransferases are generally able to use a variety of substrates, including Asp, Glu, Met, and aromatic amino acids Phe, Tyr, and Trp to donate amino groups for the transamination reaction (47, 48). Besides SAM, however, no other substrate has been found to act as an amino donor for *Mtb* DAPAS, even at concentrations of 5 mM (28).

The kinetic properties of *Mtb* DAPAS with the substrate SAM have been reported (28, 49). To investigate DAPAS catalysis further, we took advantage of the chromophore properties of the cofactor PLP to follow the half-reaction of *Mtb* DAPAS, formation of the pyridoxamine phosphate (PMP) complex, with the SAM analogues sinefungin and *S*-adenosylhomocysteine (SAH) by spectroscopic methods. SAM, sinefungin, and SAH differ in their  $\delta$  carbons; SAM and SAH have a sulfonium ion at that position (this is methylated in SAM) whereas sinefungin has an amine (Figure 4). An absorbance scan of *Mtb* DAPAS showed an absorption maximum at 420 nm, characteristic of the PLP form of the enzyme. This absorption reduced upon reaction with 1 mM

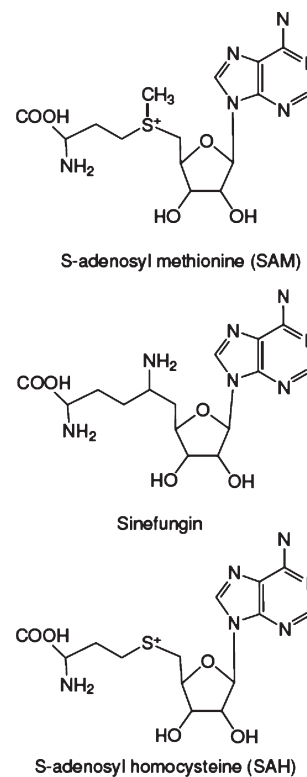


FIGURE 4: The chemical structures of SAM and its analogues sinefungin and *S*-adenosylhomocysteine.

sinefungin, resulting in an increase in absorbance at 335 nm that is characteristic of the PMP form of the enzyme. Similar results were observed when the PLP-complexed DAPAS was mixed with the product DAPA. However, the intermediate quinonoid form of the aminotransferase reaction observed at 487 nm in the *E. coli* DAPAS reaction with SAM was not detected (50). This suggests that there is no accumulation of the intermediate in the *Mtb* DAPAS reaction and that the quinonoid is quickly converted into product.

Fluorescence emission spectra of PLP-complexed *Mtb* DAPAS on excitation at 280 nm result in a peak at 335 nm. The reaction with sinefungin on excitation at 280 nm results in a decrease in this emission peak and a subsequent increase in the peak at 385 nm. The increase in emission at 385 nm represents a Förster resonance energy transfer (FRET) effect in which PMP absorbs light at 335 nm emitted by the aromatic residues and, in turn, emits at 385 nm. This result confirms PMP formation in the aminotransferase reaction with sinefungin and indicates that the SAM analogue can bind at the DAPAS active site and donate its amino group to PLP to form PMP (Figure 5). Thus, sinefungin can act as a substrate for *Mtb* DAPAS.

Similar kinetic studies with the SAM analogue SAH showed no absorption peak at 335 nm, even at concentrations up to 3 mM. This suggests that SAH is unable to donate its amino group to PLP and corresponds well with studies that demonstrate the same inability of the analogue to act as the amino donor for *E. coli* (51) and *B. sphaericus* DAPAS (8).

We also employed a single-turnover half-reaction with *Mtb* DAPAS to measure the increase in absorbance at 335 nm. We obtained the  $K_m^{\text{app}}$  and  $k_{\text{max}}$  values for sinefungin as  $0.7 \pm 0.2$  mM and 0.009/s, respectively. The equivalent values for SAM are  $0.45 \pm 0.2$  mM and 0.012/s.  $k_{\text{max}}/K_m^{\text{app}}$  for the *Mtb* DAPAS reaction with sinefungin ( $0.013 \text{ mM}^{-1} \text{ s}^{-1}$ ) are lower than those

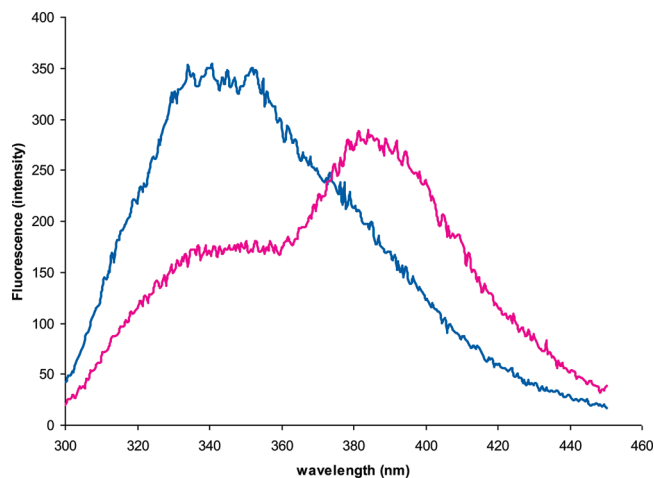


FIGURE 5: Fluorescence spectra of *Mtb* DAPAS with SAM analogue sinefungin. Fluorescence emission spectra of 12  $\mu\text{M}$  DAPAS alone (blue) and its reaction with 1 mM sinefungin (purple) were recorded at room temperature in the 300–450 nm range at 30 s.

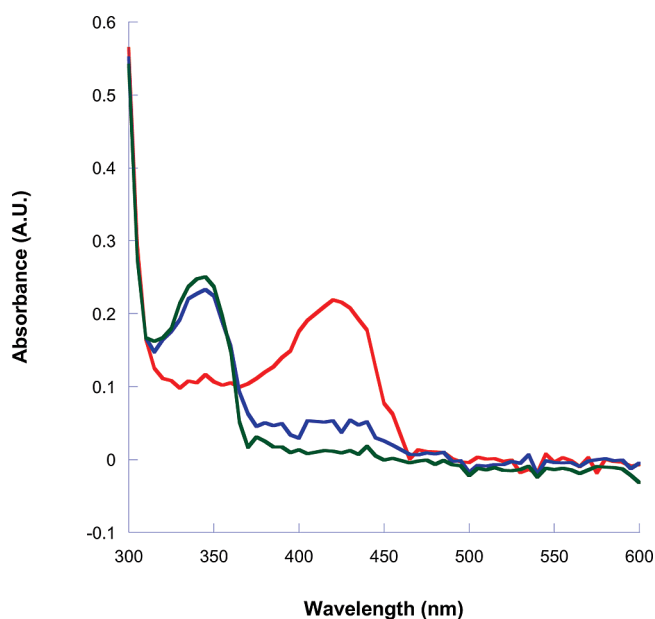


FIGURE 6: Absorption spectra of wild-type *Mtb* DAPAS with DAPA. Absorption spectra of 5  $\mu\text{M}$  DAPAS alone (red), immediately after addition of 0.1 mM DAPA (blue), and after 30 s of the reaction (green) were recorded in the range of 300–600 nm at room temperature.

obtained with SAM ( $0.03 \text{ mM}^{-1} \text{ s}^{-1}$ ), indicating that the analogue has a lower affinity for *Mtb* DAPAS than the natural substrate and that the corresponding reaction is slower.

Since aminotransferases catalyze a reversible reaction, we also studied the half-reaction of the PLP-complexed *Mtb* DAPAS with the DAPA product. Between 300 and 500 nm, the absorption spectra of this reaction show a decrease in the absorption peak at 420 nm and a subsequent increase in absorbance at 335 nm. This change in the absorption peaks represents the formation of PMP in the single-turnover reaction with DAPA (Figure 6). However, comparison of the absorbance spectra reveals that this half-reaction (0.5 mM) is much slower than the half-reaction of *Mtb* DAPAS with SAM (1 mM) (49).

**Biochemical Characterization of *Mtb* DTBS.** DTBS catalyzes the carboxylation of DAPA, closing the ureido ring to form DTB. To determine the kinetic parameters of *Mtb* DTBS

Table 1: Data Collection, Refinement, and Geometry Statistics of *Mtb* DAPAS

	Mtb-DAPAS	Mtb-DAPAS + sinefungin
PDB code	3BV0	3LV2
data collection		
space group	$P2_12_12_1$	$P2_12_12_1$
unit cell dimensions		
$a, b, c$ ( $\text{\AA}$ )	63.1, 66.5, 203.4	62.6, 83.4, 157.9
$\alpha = \beta = \gamma$ (deg)	90	90
molecules per ASU <sup>a</sup>	2	2
wavelength ( $\text{\AA}$ )	1.54	1.54
resolution range ( $\text{\AA}$ )	35–2.2	35–2.2
highest resolution bin ( $\text{\AA}$ )	2.3–2.2	2.3–2.2
observed reflections	253218	545792
unique reflections	40606	43549
completeness (%) <sup>c</sup>	92.9 (78.4)	98.7 (95.7)
average redundancy <sup>c</sup>	6.2 (3.6)	12.5 (12.3)
$I/\sigma(I)$ <sup>c</sup>	21.3 (3.5)	33.4 (7.0)
$R_{\text{sym}}$ <sup>c</sup>	0.07 (0.31)	0.07 (0.36)
refinement statistics (REFMAC)		
$R$ value (%)	19	18
$R_{\text{free}}$ value (5%)	24	23
no. of protein residues	824	836
no. of water molecules	200	309
rmsd <sup>b</sup> bond lengths ( $\text{\AA}$ )	0.009	0.009
rmsd <sup>b</sup> bond angles (deg)	1.2	1.2
average $B$ factor ( $\text{\AA}^2$ )		
Wilson plot	32.5	32.5
protein	22.5	27.3
water	21.6	27.6
PLP	19.8	18
sinefungin		31.4
Ramchandran plot (PROCHECK)		
most favored region (%)	629 (90.4)	634 (90.2)
additional allowed regions (%)	60 (8.6)	60 (8.5)
generously allowed regions (%)	3 (0.4)	5 (0.7)
disallowed regions (%)	4 (0.6)	4 (0.6)

<sup>a</sup>ASU, asymmetric unit. <sup>b</sup>rmsd, root-mean-square deviation. <sup>c</sup>Values in parentheses for the highest resolution bin.

catalysis, we carried out the coupled reaction of *Mtb* DTBS with pyruvate kinase and lactate dehydrogenase and tracked ADP formation by monitoring the decrease in NADH absorbance at 340 nm. We measured the  $K_m$  and  $V_{\text{max}}$  for ATP as 29  $\mu\text{M}$  and  $3.5 \mu\text{M min}^{-1} \text{ mg}^{-1}$ , respectively, and for DAPA as 2  $\mu\text{M}$  and  $6 \mu\text{M min}^{-1} \text{ mg}^{-1}$ , with the other substrates at saturation. The  $K_m$  for ATP in *Mtb* DTBS is four times higher than that of *E. coli* DTBS (7  $\mu\text{M}$ ) (52).

**Structure of *Mtb* DAPAS.** We solved the three-dimensional structure of the 46 kDa *Mtb* DAPAS at 2.2  $\text{\AA}$  resolution by molecular replacement using *E. coli* DAPAS as a template. Based on the Ramchandran plot, the structure has good geometry, with the exception of two residues: Lys283, which is covalently linked to PLP, and Val222. However, these residues have good electron density in both chains. The structure was refined to an  $R$ -factor of 19% and an  $R_{\text{free}}$  of 24%. The electron densities for the six histidine tag and the preceding six residues at the N-terminus are not visible, perhaps the result of flexibility in a region containing three alanine and two glycine residues. The data collection, refinement, and geometric statistics are provided in Table 1.

Like *E. coli* DAPAS, the *Mtb* DAPAS subunit structure indicates two distinct domains, the small domain, composed of amino acid residues 1–60 and 339–437, and the large domain, containing residues 61–338. The N-terminus of the small domain

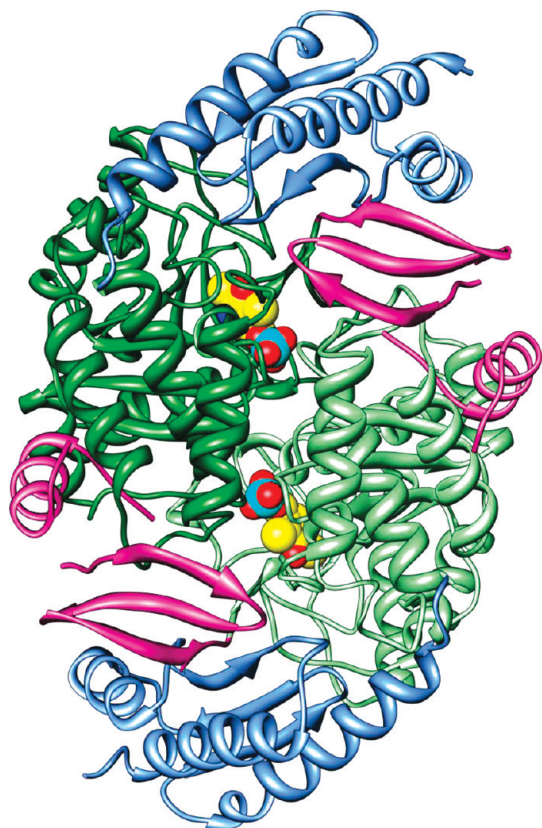


FIGURE 7: Ribbon diagram representation of the PLP-bound *Mtb* DAPAS crystal structure showing domain arrangement in the compact dimeric form of *Mtb* DAPAS. The N-terminal residues of the small domain are shown in purple and the C-terminal residues in blue. The large domain is colored in different shades of green to differentiate between the two chains. As seen, the active sites are present at the interface, 18 Å apart. This dimeric interface primarily involves the large domain interactions. PLP molecules are shown in space-filling representation (carbon atoms in yellow, oxygen atoms in red, nitrogen atoms in blue, and phosphorus atoms in aquamarine color) to indicate the position of the active site.

consists of one helix ( $\alpha 1$ ) and three antiparallel  $\beta$ -strands ( $\beta 1$ – $\beta 3$ ) connected by a long loop, and the C-terminus consists of a helix–loop–helix containing three antiparallel  $\beta$ -sheets ( $\beta 11$ – $\beta 13$ ) and three helices ( $\alpha 10$ – $\alpha 12$ ) which lie against the  $\beta$ -strands. The large domain consists of seven  $\beta$ -strands ( $\beta 4$ – $\beta 10$ – $\beta 9$ – $\beta 8$ – $\beta 7$ – $\beta 5$ – $\beta 6$ ) that are parallel with the exception of  $\beta 10$ . The  $\beta$ -strands are interconnected by helices  $\alpha 2$ – $\alpha 9$ , which also contain the cofactor binding site.

The asymmetric unit of the crystal consists of a homodimer that is formed by extensive contact between the large domains of both subunits (Figure 7). The buried surface area between these subunits is approximately 4000 Å<sup>2</sup>, 13.6% of the total subunit surface area. In this dimer formation, helix  $\alpha 2$  (Pro74–Arg85) of the large domain of subunit A is antiparallel to helix  $\alpha 2$  of the large domain of subunit B at a 2-fold axis of noncrystallographic symmetry. Both ends of the helix have one hydrogen bond contact between the main-chain oxygen of Leu84 and Asp77-OD1 through an ordered water molecule. There are several other hydrophobic interactions throughout this interface. Additional subunit contact is present in the hydrogen bond between His71-ND1 and Asp88-OD1 (2.7 Å) at the loop region, connected with helix  $\alpha 2$ . There are also hydrogen bonds between the N-terminal part of the small domain and the large domains of the two subunits at the His20-ND1–Asp116' (2.5 Å) and the His23-ND1–

Phe93' (2.8 Å) main-chain oxygens. Helix  $\alpha 1$  of the small domain from one subunit crosses over helix  $\alpha 3'$  of the large domain of the other subunit, primarily involving hydrophobic interactions with Pro, Val, and Ile residues from both. Superimposition of the two subunits of *Mtb* DAPAS using 435 C $\alpha$  atoms results in an rmsd of 0.38 Å, indicating that there is no major flexibility between the domains in contrast to what has been reported for aminotransferases of subgroup I (53, 54).

Although *Mtb* DAPAS, at 437 residues, is eight residues longer than its *E. coli* counterpart, the two share a similar overall secondary structure. The orientation and length of the *Mtb* DAPAS loop regions (rmsd for 420 C $\alpha$  atoms = 1.07 Å) Asp51–Gly52, Thr111–Asp116, Pro189–Asp196, and Ala307–Asn322, however, differ from those of the *E. coli* enzyme, as does the helix Pro197–Glu213 with a transition of 2 Å. Furthermore, there are a large number of interactions unique to *Mtb* DAPAS which are not observed in *E. coli* DAPAS. These include a salt bridge between Arg246 and Glu204 (2.7 and 3.1 Å) and hydrogen bonds between Tyr195-OH–Asp239-OD2–Ser200- $\gamma$ O, Lys105-NZ–Asp109 (2.9 and 2.7 Å), and Trp45-NE1–Glu418-OE2 (3 Å).

**Analysis of DAPAS Active Site Architecture.** The *Mtb* DAPAS active site is a 24 Å deep pocket with an entrance of 22 Å × 23 Å that narrows to 14 Å × 10 Å at the bottom. The pocket is composed of loop regions Pro24–Ser34, Arg156–Asp160, Gln224–Gly228, Arg400–Arg403, Ala307'–Asn322', and Met87'–His97' from the small and large domains of one subunit and the large domain of the neighboring subunit to accommodate two dissimilar substrates, SAM or KAPA/DAPA (the prime (') indicates the residues in the adjacent subunit). Residues from both chains make up the catalytic site, and the two active sites are approximately 18 Å apart. The entrances to the cavities are at opposite sides of the dimer axis (Figure 7). In the *Mtb* structure, the loop at the entrance of the active site (Tyr25–Val33) and the long loop that lines the active site (Gly307'–Pro316') are in disorder. The latter has four alanine and three glycine residues in the sequence at the entrance of the tunnel (AGAAGALMHGP), rendering it flexible on solvent exposure. The contrasting lack of flexibility at the dimer interface of the *E. coli* structure may explain its higher efficiency, although there are also 13 residues lining the *Mtb* DAPAS active site that are not conserved in the *E. coli* enzyme.

The continuous electron density between PLP and Lys283 in the *Mtb* DAPAS structure highlights an inherent feature of aminotransferases, the covalent link between the cofactor and the N $\epsilon$  group of the conserved Lys283. Like *E. coli* DAPAS, *Mtb* DAPAS is a PLP fold type I enzyme in which all residues interacting with PLP are conserved.

**DAPAS Substrate Binding Site.** The binding site of the amino donor in the DAPAS active site has not been reported to date. Initial crystallization trials of the *Mtb* DAPAS with SAM, both by soaking and cocrystallization, were not fruitful. Our spectrophotometric analysis demonstrates that the SAM analogue sinefungin can act as a substrate for this enzyme, with a  $K_m^{\text{app}}$  of 0.7 ± 0.2 mM for the first half-reaction ( $K_m^{\text{app}}$  for SAM is 0.45 ± 0.2 mM). Therefore, we determined the crystal structure of *Mtb* DAPAS complexed with sinefungin at 2.2 Å and refined to an  $R$ -factor of 18% and an  $R_{\text{free}}$  of 23%. Sinefungin occupies the extra electron density adjacent to the C4' atom of PLP at the active site of DAPAS chain A. In chain B the electron density for sinefungin is broken due to disorder. In the structure of subunit A, PLP is covalently attached to Lys283, and there is nothing in the PMP form that would be indicative of product formation.

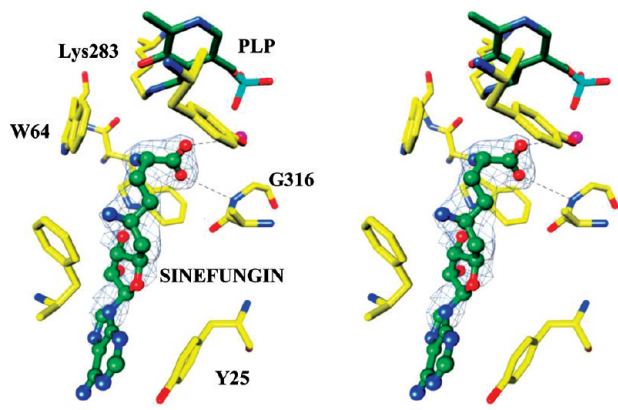


FIGURE 8: Precatalytic binding of sinefungin at the *Mtb* DAPAS active site. This figure shows the stereoview of the pre-catalytic state of sinefungin binding at the catalytic site of the *Mtb* DAPAS. The electron density ( $2F_o - F_c$ ) for sinefungin (light blue) is contoured at the  $1\sigma$  level. Most of the surrounding residues at the active site have been shown. Arg315 has been truncated for the clarity of the figure. The amino donor sinefungin is shown in ball and stick form, cofactor PLP is shown in green, and the surrounding residues are shown in yellow stick representation. The water molecule is shown in purple. Oxygen atoms are shown in red, nitrogen atoms are in blue, and phosphorus atoms are in cyan.

This may result from the short soaking period for sinefungin (10 mM for 45 min); longer soaking or higher substrate concentrations resulted loss of diffraction. The sinefungin-bound *Mtb* DAPAS structure thus depicts the pre-catalytic state of substrate binding (Figure 8).

From chain A the amino group of sinefungin points toward the internal aldimine in this structure, oriented to form the external aldimine complex required for subsequent amino group donation. The carboxy oxygen atoms of sinefungin form hydrogen bonds with the main-chain amide of Gly316' (3.4 Å) and the hydroxyl group of Tyr157 via a water molecule at the active site. The five-membered aliphatic chain of sinefungin spans the entire length of the active site pocket and forms van der Waals contacts with the side chains of Trp64, Trp65, and Phe402. At the entrance of the active site pocket, the electron density for part of the ribose sugar and the adenine ring of sinefungin is highly disordered from complete solvent exposure. A loop (Ser26–Ala32) near the entrance of the pocket is also disordered, similar to that of the native structure. However, unlike the apo structure, the loop region in chain A (Gly307'–Pro316') lining the active site at the dimer interface of the sinefungin structure is ordered from the presence of the ligand. Tyr25, which may be involved in a stacking interaction with the adenine ring of sinefungin, is also more ordered than it is in the PLP enzyme structure. Support for the interaction of Tyr25 with the adenine ring is analogous to the interaction of Tyr85 in the structure of 1-aminocyclopropane-1-carboxylate (ACC) synthase complexed with the amine-oxy SAM analogue [2-(aminoxy)ethyl](5'-deoxyadenosin-5'-yl)-(methyl)sulfonium (AMA) (PDB code: 1M4N) (55).

Superimposition of the sinefungin-bound *Mtb* DAPAS structure on the PLP-bound structure shows that the enzyme does not undergo major conformational changes (the rmsd for 429  $C_\alpha$  atoms is 0.3 Å) except for movement of the side chains of Trp64, Trp65, Met409, and Phe402 to accommodate sinefungin at the active site pocket; this may be partially accounted for by the flexibility of subunit B. The indole side chains of both Trp64 and Trp65 rotate 90°, causing the side chain of Met409 to move by 2 Å. Comparison of these structures provides the putative binding

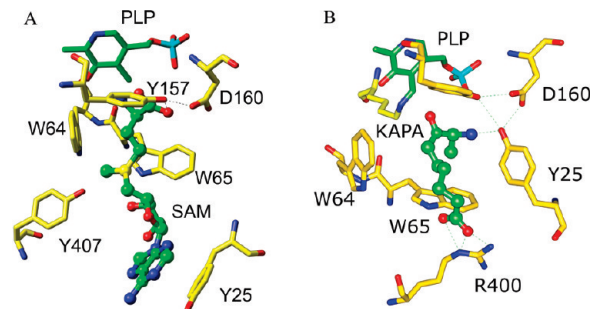


FIGURE 9: Substrate recognition at the *Mtb* DAPAS active site. (A) Interaction of amino group donor SAM, shown in green ball and stick form, with DAPAS. The DAPAS active site residues are shown in yellow stick form. The amino group of SAM points toward PLP, the carboxy group interacts with the network of Tyr157 and Asp160, and the Tyr25 residue forms a stacking interaction with the adenine ring of SAM. Trp64 and Trp65 have changed their orientations to accommodate SAM at the active site. (B) Interaction of amino group acceptor KAPA, shown in green ball and stick form, with DAPAS. KAPA binds at a similar position as SAM at the active site. Here, Tyr25 changes its orientation to form a hydrogen bond with the amino group of KAPA. The carboxy group of KAPA forms a salt bridge with Arg400.

site for SAM in a wide active site cleft. We speculate that the change in the unit cell dimension of the sinefungin-bound DAPAS *Mtb* structure ( $a = 62.6$  Å,  $b = 83.4$  Å,  $c = 157.9$  Å,  $\alpha = \beta = \gamma = 90^\circ$ ) compared to the PLP-bound structure ( $a = 63$  Å,  $b = 66.5$  Å,  $c = 203.4$  Å,  $\alpha = \beta = \gamma = 90^\circ$ ) is the result of crystal packing.

Based on the pre-catalytic sinefungin-bound structure, we further modeled SAM to a position 2 Å inside the *Mtb* DAPAS active site pocket (Figure 9A). Movement of SAM inside the active site would allow its amino group to form a Schiff's base with the C4' group of PLP. The carboxy oxygen atoms of SAM would then interact with the hydrogen bond network of Tyr157–OH–Asp160–OD2, the aliphatic chain would span the hydrophobic active site pocket, and the adenine ring would form a stacking interaction with the phenol ring of Tyr25. Most subgroup II aminotransferases, in contrast, have hydrogen bonds between the carboxy groups of the amino donor and arginine residues in the active site (56, 57). The sulfonium ion of SAM may hydrogen bond with the hydroxyl group of the conserved Tyr407, and the oxygen atom of the ribose sugar may form similar interactions with Arg400 and the N-atom of Trp65 imidazole ring.

We were unable to produce *Mtb* DAPAS crystals complexed with KAPA, the amino group acceptor. Therefore, to locate the substrate binding site, we superimposed the KAPA-bound *E. coli* DAPAS structure (PDB code: 1QJ3) (15) on the *Mtb* enzyme structure. In the *E. coli* DAPAS structure, KAPA is bound to the PLP form of the enzyme, an unproductive enzyme complex (15). Based on this superimposition, the 7-keto group of KAPA points toward the internal aldimine and is approximately 2.6 Å, and the 8-amino group forms a hydrogen bond with the hydroxyl group of Tyr25 (2.5 Å) as well as with the main-chain oxygen of Gly316' (2.5 Å) in *Mtb* DAPAS. Conserved residue Tyr25 is thought to stabilize KAPA binding by forming a hydrogen bond with the amino group. The carboxyl group of KAPA has specificity for the conserved Arg400, whose side chain moves 3 Å toward KAPA to form a salt bridge (2.6 and 3.15 Å) and break the hydrogen bond between itself and Thr389. The movement of the Arg400 guanidinium group in response to KAPA binding at the active site is not seen with sinefungin binding. The rest of the KAPA aliphatic chain is within van der Waals distance to active

Table 2: Data Collection, Refinement, and Geometry Statistics of *Bs* DAPAS

	<i>Bs</i> -DAPAS	<i>Bs</i> -DAPAS + PLP	<i>Bs</i> -DAPAS + PLP + KAPA
PDB code	3DRD	3DOD	3DU4
data collection			
space group	$P2_1$	$P2_1$	$P2_1$
unit cell dimensions			
$a, b, c$ (Å)	58.1, 102.8, 74.5	58.1, 102.8, 74.5	57.7, 105.1, 75.1
$\alpha = \gamma$ (deg)	90	90	90
$\beta$ (deg)	105.1	105.1	105.2
molecules per asymmetric unit	2	2	2
wavelength (Å)	1.54	1.54	1.54
resolution range (Å)	35–2.2	35–1.9	30–2.2
highest resolution bin (Å)	2.3–2.2	1.97–1.9	2.28–2.2
observed reflections	279606	397953	184127
unique reflections	41693	65688	43651
completeness (%) <sup>b</sup>	93 (63.5)	99.1 (98)	99.4 (95)
average redundancy <sup>b</sup>	6.7 (4.4)	6.1 (6.2)	4.2 (3.5)
$I/\sigma(I)$ <sup>b</sup>	26.1 (3.8)	10.5 (2.8)	7.2 (2.8)
$R_{\text{sym}}$ <sup>b</sup>	0.063 (0.32)	0.072 (0.48)	0.11 (0.37)
refinement statistics (REFMAC)			
$R$ value (%)	20	20	20
$R_{\text{free}}$ value (5%)	26	24	26
no. of protein residues	836	833	894
no. of water molecules	250	385	261
rmsd <sup>a</sup> bond lengths (Å)	0.009	0.009	0.01
rmsd <sup>a</sup> bond angles (deg)	1.28	1.26	1.4
average $B$ factor (Å <sup>2</sup> )			
Wilson Plot	32.5	33.8	31.5
protein	27.6	48.2	28.8
water	22.7	48.7	25.3
PLP		42.6	27.2
KAPA			38.2
Ramachandran plot (PROCHECK)			
most favored region (%)	654 (89.1)	658 (90.0)	681 (87.3)
additional allowed regions (%)	71 (9.7)	68 (9.3)	94 (12.1)
generously allowed regions (%)	5 (0.7)	1 (0.1)	1 (0.1)
disallowed regions (%)	4 (0.5)	4 (0.5)	4 (0.5)

<sup>a</sup>rmsd, root-mean-square deviation. <sup>b</sup>Values in parentheses for the highest resolution bin.

site residues Tyr25, Trp64, Tyr157, and Phe402 (Figure 9B). Analogous to sinefungin binding, modeled KAPA binding to DAPAS does not result in major conformational changes (rmsd = 0.3 Å for 429  $C_{\alpha}$  atoms) apart from the movement of a few residues' side chains (Trp64, Trp65, and Met409). Higher concentrations of KAPA ( $14 \pm 2 \mu\text{M}$ ) inhibit DAPAS by forming a dead end complex in the active site (28). These data suggest that KAPA and SAM, despite differences in size and other characteristics, bind at the same place in the active site.

**Possible DAPAS Substrate Recognition.** Aminotransferases use two main mechanisms, alone or in combination, to identify dual substrates at the same active site: the “induced fit” mechanism (58, 59), in which the conformation of the active site changes on substrate binding, and the “lock and key” mechanism (60), in which the active site and substrate are complementary to each other. Subgroup I enzymes aspartate aminotransferase (53, 54) and glutamine phenylpyruvate aminotransferase (48) employ an induced fit mechanism, with large movement of the small domain ( $13^\circ$  rotation) as a rigid body for substrate recognition. Other transaminases such as lysine aminotransferase use the glutamate switch (61), while tyrosine aminotransferase (57) and GABA aminotransferase (56) use the arginine switch. Acetylornithine aminotransferase employs a combination of a lock and key and induced fit mechanisms for recognition of its acetylornithine and  $\alpha$ -ketoglutarate substrates (57).

The reaction catalyzed by *Mtb* DAPAS proceeds via a ping-pong bi–bi reaction mechanism (28). The enzyme differs from most aminotransferases in that its amino donor, SAM, does not resemble its amino acceptor, KAPA. To accommodate such disparate substrates, DAPAS appears to use a local induced fit mechanism in which certain residues at the active site change their side chain orientations but avoid large conformational changes in the form of domain movement. When SAM binds at the DAPAS active site, its amino group forms a Schiff's base with PLP and its carboxy group hydrogen bonds to the Tyr157–OH–Asp160–OD2 network. The conserved Tyr25 residue changes the orientation of the phenol ring by approximately  $180^\circ$  to provide a platform for stacking interactions with the adenine ring. Following the release of SAM, KAPA binds at the same active site region of the PMP form of DAPAS, and the Tyr25 side chain again changes its orientation by rotating  $90^\circ$  clockwise to form a hydrogen bond interaction with the 8-amino group of KAPA. This bond positions KAPA to accept the amino group from PMP. In response to this interaction, the guanidinium group of Arg400 moves 3 Å toward KAPA to form a salt bridge with the carboxy group of the substrate (Figure 9B).

**Variation in the Mode of DAPAS Substrate Binding.** To confirm the role of Tyr25 in *Mtb* DAPAS substrate recognition suggested by our structural studies, we constructed a Y25A mutant and spectrophotometrically followed the half-reactions

of the mutant enzyme with SAM and DAPA. Compared to the native protein, the Y25A mutant does not show detectable activity at 335 nm with SAM, even up to concentrations of 3 mM, and shows approximately 70% reduced activity with high concentrations of DAPA (0.5 mM). These results support a role for *Mtb* DAPAS Tyr25 in both a stacking interaction with the adenine ring of SAM and proper positioning of KAPA for amino group acceptance.

In *E. coli* DAPAS, the Tyr to Phe mutation results in a 60-fold reduction in enzyme activity in the second half of the reaction with DAPA but has no effect on the first half of the reaction with SAM (13) because Phe can still stack with SAM's adenine ring. Interestingly, based on sequence alignment of different DAPAS proteins, *Bacillus* species *B. subtilis* and *B. cereus* as well as *Brucella melitensis* and *Aquifex aquenox* have a Phe residue in this position of the protein sequence, raising the question of how substrate binding, especially KAPA binding, occurs in these organisms.

To investigate alternative mechanisms of KAPA binding, we solved the crystal structure of the *B. subtilis* DAPAS apoprotein, its PLP-bound complex, and its ternary complex with PLP and KAPA at resolutions of 2.2, 1.9, and 2.2 Å, respectively (Table 2). Sequence alignment of these enzymes shows that *B. subtilis* DAPAS has a 32% sequence identity with *Mtb* DAPAS and 33% with the *E. coli* enzyme. The overall structure of *B. subtilis* DAPAS is similar to its *Mtb* and *E. coli* counterparts, with a pairwise rmsd of ~1 Å for 325 C $\alpha$  atoms. Unlike the *Mtb* and *E. coli* DAPAS, however, a large part of the active site (Lys143–Glu172) is completely disordered in both chains. PLP binding does not help to order this region of the active site. However, we were able to trace the active site of the enzyme using the KAPA-bound structure in which electron density for these 29 residues is clearly visible in both chains.

In the unproductive KAPA-bound *B. subtilis* structure, the carboxy group of the substrate forms a salt bridge with the guanidinium group of Arg403 (2.8 Å). The Arg residue moves backward 2.2 Å, in contrast to *E. coli* DAPAS. In the absence of Tyr17, the amino group of the KAPA hydrogen binds to the OH group of Tyr146 (2.8 Å) and to the main-chain oxygen of Gly315' (2.65 Å) while maintaining the hydrogen bond network of Tyr146-OH–Asp149-OD2. Comparing this to the KAPA-bound *E. coli* DAPAS, these interactions result in a 1 Å shift in the active site's KAPA binding position where it approaches Tyr146 for hydrogen bond formation (Figure 10). The substrate hence stabilizes the loop region of the *B. subtilis* active site. In the *E. coli* Y17F mutant structure (PDB code: 1S0A) (13), a water molecule fills the role of the hydroxyl group of Tyr17 in the active site, further indicating the importance of the Tyr157–Asp160–Tyr25 hydrogen bond network in maintaining active site structure. We note that two consecutive Trp residues and a Gly are present in the *Mtb* and *E. coli* DAPAS active sites, replacing the Val53, Trp54, and Leu82' residues found in the *B. subtilis* enzyme. The void created by Val53 at the active site is filled by Leu82' from the neighboring subunit. Thus the *B. subtilis* DAPAS structures shed light on the maintenance of enzyme activity in the absence of Tyr25. Analysis of a DAPAS phylogenetic tree shows that the *B. subtilis* enzyme evolved long before *Mtb* or *E. coli* DAPAS, suggesting that the Tyr residue may represent a recent adaptation toward greater efficiency.

**Search for an *Mtb* DAPAS Inhibitor.** PLP is a cofactor for several enzymes that catalyze diverse reactions, some of which are implicated in human disease. Part of the mechanism by which

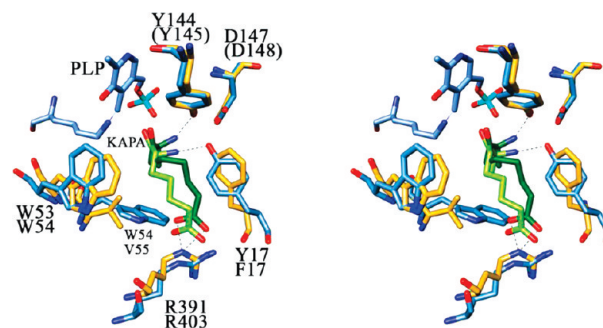


FIGURE 10: Stereoview of KAPA binding at the *B. subtilis* DAPAS active site. Superimposition of KAPA-bound *E. coli* DAPAS (PDB code: 1QJ3) in blue and *B. subtilis* DAPAS in orange shows the binding pattern of KAPA in the absence of Tyr17. KAPA is represented in stick form, dark green in *E. coli* and light green in *Bacillus*. There is a transition of KAPA in *Bacillus* by approximately 1 Å for hydrogen bond formation with Tyr145.

these reactions occur involves aldimine formation with PLP. This interaction is the target for many of the most potent inhibitors against this class of enzymes.

The natural antibiotic amikacin irreversibly inhibits *Mtb* DAPAS *in vitro* ( $K_i = 12 \pm 2 \mu\text{M}$ ) (16) and is effective against *Mtb* in cell culture (24). To examine the mechanism of irreversible inhibition, we superimposed the *cis*-amikacin-bound structure of *E. coli* DAPAS (PDB code: 1MLY) (16) on the *Mtb* enzyme. In this model, amikacin occupies the same position as KAPA, forming an irreversible aromatic adduct with PLP by a covalent bond with the C4' carbon atom of the cofactor and tilting it at an angle of 17°. Hydrophobic interactions with Trp64, Trp65, and Phe402 further stabilize the aromatic adduct. Tyr25, however, does not seem to form hydrogen bonds with the amino group of amikacin.

The side chain of Arg400 translates 3 Å to form a salt bridge with the carboxy group of the antibiotic (2.8 and 2.5 Å) and provides specificity to the inhibition. This may be the reason that drugs such as cycloserine (62) and gabaculine (63, 64) do not inhibit *Mtb* DAPAS despite working well against alanine racemase ( $K_i = 360 \mu\text{M}$ ) and GABA aminotransferase ( $K_i = 2.86 \mu\text{M}$ ), respectively, though they employ similar mechanisms of inhibiting aromatic adduct formation with PLP (28). We also find that vigabatrin, a potent inhibitor of GABA aminotransferase and an effective epilepsy treatment (65), is ineffective against *Mtb* DAPAS, possibly because the compound is not long enough to form bonds with both PLP and Arg400. There are no other Arg residues lining the active site of the enzyme to provide specificity by interacting with the carboxy groups of vigabatrin covalently bonded to PLP.

We are currently pursuing the design of more effective inhibitors of *Mtb* DAPAS using a structure-based drug design approach including virtual screening experiments of the rigid active site against commercially available libraries of drug-like compounds.

**Structure of *Mtb* DTBS.** In the penultimate step of biotin biosynthesis, DTBS carboxylates DAPA to form the ureido ring of dethiobiotin (DTB) in an ATP- and magnesium-dependent manner. We solved the crystal structure of the *Mtb* enzyme using single anomalous dispersion (SAD) with the lanthanide metal samarium at Cu wavelength (1.54 Å). The phases obtained were further extended to high-resolution native data of 1.85 Å and refined to a final  $R$ -factor of 22% and an  $R_{\text{free}}$  of 26%. On PROCHECK evaluation (43), no outliers were apparent in the

Table 3: Data Collection, Refinement, and Geometry Statistics of *Mtb* DTBS

	DTBS-Sm	native DTBS	DTBS + DAPA	DTBS + KAPA	DTBS + DTB + phosphate
PDB code		3FGN	3FMF	3FMI	3FPA
data collection					
space group	$P2_12_12_1$	$P2_12_12_1$	$P2_12_12_1$	$P2_12_12_1$	$P2_12_12_1$
unit cell dimensions					
$a, b, c$ (Å)	55.9, 104.2, 152.3	55.4, 104.7, 151.4	55.3, 103.8, 151.5	55.3, 105.1, 151.6	55.1, 104.5, 151.1
$\alpha = \beta = \gamma$ (deg)	90	90	90	90	90
molecules per asymmetric unit	4	4	4	4	4
wavelength (Å)	1.54	1.54	1.54	1.54	1.54
resolution range (Å)	22–2.6	32–1.85	31.5–2.05	30–2.18	35–2.3
highest resolution bin (Å)	2.7–2.6	1.95–1.85	2.12–2.05	2.26–2.18	2.4–2.3
observed reflections	397900	312728	270190	640379	315813
unique reflections	52748	73844	50636	46066	39525
completeness (%) <sup>b</sup>	100 (99.8)	99 (93.7)	91.2 (80.6)	97.6 (96.3)	99.9 (99.8)
average redundancy <sup>b</sup>	7.5 (7.3)	4.2 (2.3)	5.3 (4.9)	13.9 (13.5)	8.0 (7.7)
$I/\sigma(I)$ <sup>b</sup>	9.5 (4.9)	17.2 (1.4)	29.5 (8.4)	38.0 (7.3)	17.0 (2.0)
$R_{\text{sym}}$ <sup>b</sup>	0.15 (0.41)	0.16 (0.54)	0.05 (0.17)	0.06 (0.39)	0.05 (0.21)
refinement statistics (REFMAC)					
$R$ value (%)		21	20	21	21
$R_{\text{free}}$ value (5%)		25	24	27	26
no. of protein residues		907	904	904	904
no. of water molecules		320	298	195	180
rmsd <sup>a</sup> bond lengths (Å)		0.01	0.01	0.016	0.012
rmsd <sup>a</sup> bond angles (deg)		1.3	1.3	1.8	1.6
average $B$ factor (Å <sup>2</sup> )					
Wilson plot		31.5	25.3	40.4	45.3
protein		35.5	23.3	36.7	37.2
water		31.7	21.3	31.7	32.1
DAPA			22.5		
KAPA				34.7	
DTB					44.0
PO <sub>4</sub>					33.2
Ramachandran plot (PROCHECK)					
most favored region (%)		726 (95.2)	714 (95.1)	712 (94.9)	696 (92.4)
additional allowed regions (%)		36 (4.7)	36 (4.8)	37 (4.9)	50 (6.6)
generously allowed regions (%)		1 (0.1)	1 (0.1)	1 (0.1)	5 (0.7)
disallowed regions (%)		0	0	0	0

<sup>a</sup>rmsd, root-mean-square deviation. <sup>b</sup>Values in parentheses for the highest resolution bin.

disallowed region of the Ramachandran plot. The data collection, refinement, and geometry statistics of this enzyme are provided in Table 3.

The asymmetric unit of the *Mtb* DTBS structure has four molecules, and each pair of molecules (chains A and B and chains C and D) forms a dimer. The electron density for the entire polypeptide chain is well-defined in all four subunits. Each subunit of the 226 amino acid DTBS consists of one globular domain containing seven parallel  $\beta$ -sheets ( $\beta 3$ - $\beta 2$ - $\beta 4$ - $\beta 1$ - $\beta 5$ - $\beta 6$ - $\beta 7$ ) interconnected with  $\alpha$ -helices. Like other synthetases, the structure consists of the classical P-loop motif (also called the Walker A motif), Gly8-X-Gly10-X-Gly12-Val13-Gly14-Lys15-Thr16, which binds the phosphate group of the nucleotide. Here, the motif is in a loop region between strand  $\beta 1$  and helix  $\alpha 1$  at the N-terminus of the protein. There is also a Walker B motif at strand  $\beta 4$  (Leu104-Thr105-Leu106-Val107-Glu108). The dimer formation occurs in a buried surface area of approximately 1300 Å<sup>2</sup> (7.5% of total surface area of the dimer). The 37.2 Å elongated dimer interface mainly involves the  $\alpha 3$  (Pro74-Ala81),  $\alpha 6$  (Gly144-Gln159), and  $\alpha 7$  (Leu177-Ile189) helices, the loop (Gly109–Leu124) between strand  $\beta 5$  and helix  $\alpha 5$ , and the phosphate-binding loop (Thr9–Gly14) between strand  $\beta 1$  and helix  $\alpha 1$  of both the subunits (the prime (') indicates the residues in the adjacent subunit). There are six helices present at the

subunit–subunit interface, the inner helices,  $\alpha 5$  and  $\alpha 5'$ , of both subunits, and the outer helices,  $\alpha 6$  and  $\alpha 3'$  and  $\alpha 3$  and  $\alpha 6'$ , which are perpendicular to each other. Because the dimer forms at the 2-fold noncrystallographic axis, all residual contact occurs twice. The interface of helices  $\alpha 5$  and  $\alpha 5'$  involves a stacking interaction of the imidazole rings of His148 and His148'. The interface of helices  $\alpha 3$  and  $\alpha 6'$  makes hydrogen bond contacts between Arg188-NH2 and Glu79'-OE2 (3.5 Å) and hydrophobic interactions with Met72, Leu177, and Val178. Other interactions at the dimer interface include hydrogen bonding between the Thr9 main-chain oxygen of the P-loop and His148-NE2 (2.7 Å), hydrogen bonding between the Asn147-OD1 of one monomer and the main-chain amide nitrogen of Leu114 of the other (2.9 Å), and a salt bridge between Arg125 and Glu154 of both chains (2.85 and 3.0 Å). Superimposition of chain A on chain B of the dimer shows little variation in the overall structure (rmsd = 0.62 Å), indicating a lack of flexibility.

*Binary Complexes of DTBS with DAPA and with Its Analogue KAPA.* To understand the substrate-binding mode at the *Mtb* DTBS active site, we soaked the enzyme crystals with the DAPA substrate. The 2.2 Å crystal structure of *Mtb* DTBS reveals a long, distinct density at the dimer interface that fits DAPA in all four chains of the asymmetric unit as well as additional electron density attached to the N7 atom of DAPA

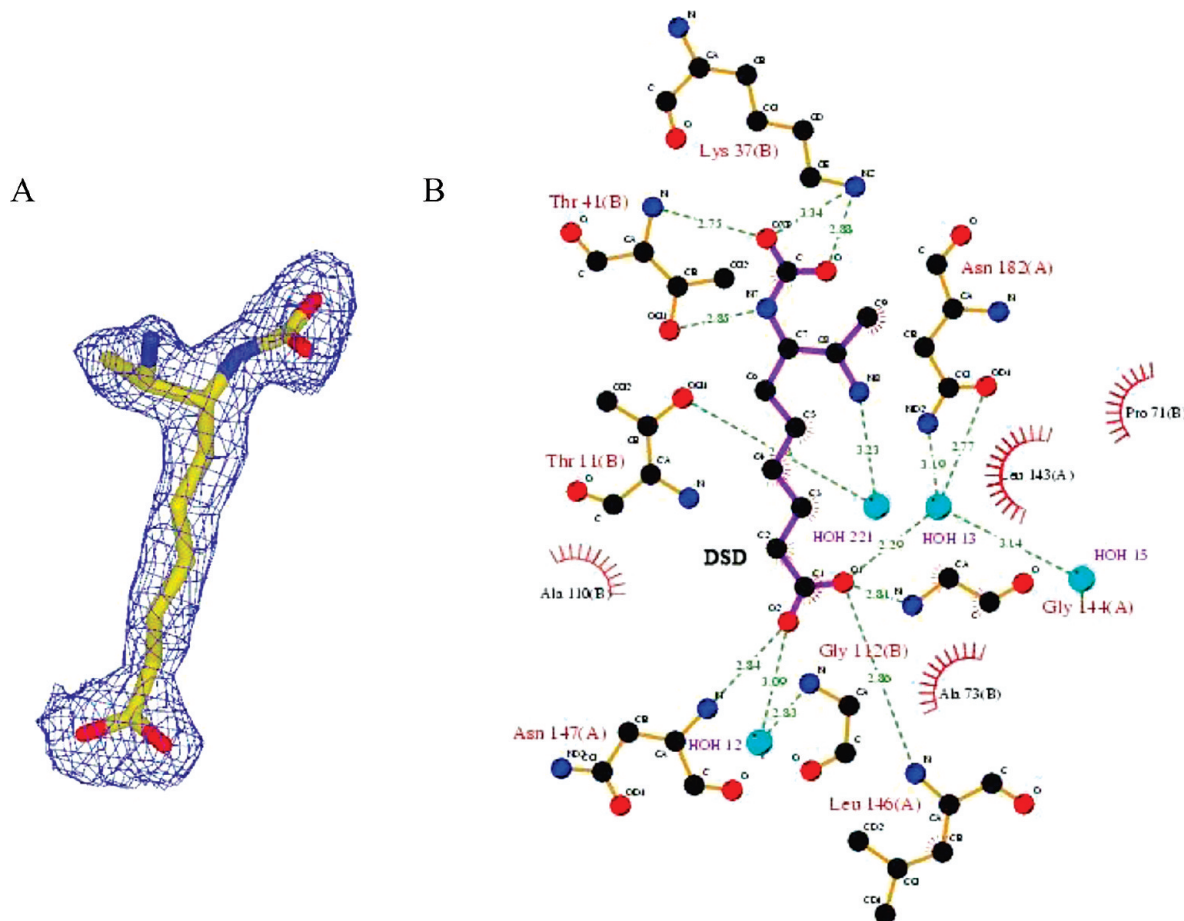


FIGURE 11: Mode of DAPA-carbamate binding at the *Mtb* DTBS active site. (A) There is clear electron density ( $2F_o - F_c$ ) for DAPA-carbamate, shown in yellow stick form, at the  $3\sigma$  level. (B) Residues interacting with the substrate DAPA-carbamate in the DTBS active site are shown in this figure. This plot has been prepared using Ligplot (72). The protein residues are colored orange, and the ligand DAPA-carbamate is colored purple. The water molecules are colored cyan. Hydrogen bonds are shown in green dotted lines. Hydrophobic interactions are shown in brick red sunbursts. Atoms are colored by type (C, black; O, red; N, blue; S, yellow).

that fits the carbon dioxide molecule (Figure 11). The carboxy group of the carbamate occupies the position of the water molecule (W11) at the active site of the apo structure, and the carboxy oxygen atoms are within hydrogen bond distance to the catalytic Lys37 (3 and 3.4 Å) and to the Thr41 main-chain amide nitrogen (2.8 Å). There are hydrogen bond links between the N7 atom of DAPA-carbamate and Thr41-OG1 (2.89 Å) and between the N8 atom and Thr11-OG1, both through water molecules. The long aliphatic chain of this unnatural amino acid spans the active site pocket, which is located at the dimer interface and is composed of a stretch of residues from helix  $\alpha 6$  (Leu143'–Asn147') and loops Pro71–Pro74 and Ala110–Gly112.

One of the C1-carboxy oxygen atoms of DAPA coordinates with the main-chain amide of Leu146' (2.78 Å) and an ordered water molecule (2.6 Å), while the other hydrogen bonds with the main-chain amide of Asn147' (2.6 Å) in helix  $\alpha 6$  of the adjacent subunit and with the  $\alpha 7$  helix's Asn182'-OD1 through a neighboring water molecule (3 Å). This water molecule is absent from the active site of the *Mtb* DTBS apo structure. The presence of the water molecule causes a peptide flip at Gly111 of the loop region 110–112, a phenomenon not seen in *E. coli* DTBS despite identical sequence in the 106–112 region (LVEGAGG). Finally, Tyr187' in helix  $\alpha 6$  of the substrate-bound *E. coli* structure, replaced by Asn182' in the corresponding *Mtb* structure, changes its side chain orientation approximately 90° upon DAPA binding and hydrogen bonds with the carboxy oxygen of DAPA.

Similar interactions are also visible for KAPA at the DTBS active site. As evident from the weak electron density for KAPA and its high *B* factor, however, the occupancy of KAPA (0.5) is much lower than DAPA (1.0) at the active site of all four chains of the asymmetric unit. The low occupancy of KAPA suggests that it may have low affinity as a substrate for DTBS.

The KAPA-bound enzyme structure has a sulfate ion from the crystallization solution bound at the P-loop (Gly8–Thr16), mimicking the  $\beta$ -phosphate of the nucleotide. The 7-keto oxygen atom of KAPA points toward the sulfate ion with an ordered water molecule occupying a similar position to the  $\gamma$ -phosphate of the nucleotide at the active site (3.2 Å). The N8 atom of KAPA forms a hydrogen bond with Thr41-OG1 (3 Å) at the active site. Thus, KAPA and DAPA occupy similar positions in the hydrophobic pocket of the enzyme, away from the P-loop.

The substrate-bound *Mtb* DTBS structures illustrate that the first substrate, DAPA, can bind to the enzyme in the absence of the second substrate, ATP. They may also indicate *Mtb* DTBS specificity for N7-DAPA-carbamates as the crystallization conditions did not introduce bicarbonate.

*DTBS Interactions with ATP/ADP.* To further characterize the interaction of ATP with *Mtb* DTBS and the resulting conformational changes upon binding, we attempted to determine the crystal structures of the enzyme bound to ADP or to the ATP analogues AMP-PCP and ATP- $\gamma$ -S. Only partial electron density for these entities at the active site was visible, phosphate

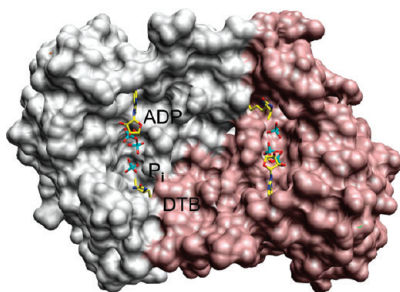


FIGURE 12: Surface representation of the *Mtb* DTBS active site. The *Mtb* DTBS active site is composed of both subunit A, colored in gray, and subunit B, colored in rose brown. DTB is positioned inside the pocket and is anchored to the other subunit. Adjacent to DTB,  $P_i$  and ADP are completely exposed to the solvent. DTB,  $P_i$ , and ADP molecules are shown in stick form.

ions were clear at the P-loop, but electron density for the rest of the molecules was poorly defined. Hence, to pinpoint the residues involved in the interactions of the nucleotides at the active site, we superimposed the ADP-complexed *E. coli* DTBS structure (PDB code: 1DAM) (18) on the *Mtb* structure. Surface representation of the *Mtb* DTBS active site shows that the 17 Å long, nucleotide-binding region is completely exposed to solvent, resulting in disordered electron density for ATP/ADP (Figure 12). This might be due to *Mtb* variation in the conformations of the Gln168–Val176 loop region and of Leu196–Asp204 near the adenine ring binding pocket. A unique feature of the loop region is the presence of multiple proline residues, Pro172, Pro174, and Pro175, which likely decrease loop flexibility. The only apparent interaction of DTBS with the nucleotide ribose sugar occurs between the  $O2'$  atom and the carboxy group of Glu52 via a water molecule. This glutamic acid residue is present on helix  $\alpha 2$  and is 5.3 Å closer to the active site than its *E. coli* counterpart, Glu211. The *E. coli* DTBS Glu211 residue makes direct hydrogen bond contact with the  $O2'$  of the nucleotide ribose sugar and is present in the loop region (Trp209–Glu212) between strand  $\beta 7$  and helix  $\alpha 9$ . This interaction orders the ADP-bound *E. coli* DTBS loop region (PDB code: 1DTS), an event that has been reported for other GTPases (66, 67). Intriguingly, the unliganded *Mtb* DTBS structure also displays clear density for this loop, possibly the contribution of the long helix  $\alpha 7$  that is absent in the *E. coli* enzyme and resides just behind the loop region. The nitrogen atoms of the adenine ring make hydrogen bond interactions with the peptide loop (Leu196–Gly199), the N1 atom with the main-chain amide of Gly199 (2.7 Å), and the N7 atom with the main-chain oxygen of Gly169 (2.7 Å). Superimposition of the ADP-complexed *E. coli* DTBS structure on the *Mtb* enzyme structure thus shows that the solvent-exposed nucleotide-binding site is located adjacent to the hydrophobic DAPA binding pocket in *Mtb* DTBS.

DAPA and ATP have distinct binding sites in both *E. coli* and *Mtb* DTBS. When the  $\gamma$ -phosphate of ATP is bound to one monomer, the distance (23.8 Å) to the carboxy group of the DAPA-carbamate bound to the same monomer is too far to perform the catalytic reaction. We therefore hypothesize that the two DTBS active sites are composed of two subunits each such that the enzyme reaction combines the ATP from one monomer with the DAPA substrate from the other. The active sites of the enzyme are approximately 13 Å apart at the dimer interface and have entrances facing the same side (Figure 12).

Substrate binding does not produce drastic changes in DTBS conformation. However, there are local conformational changes

in the orientations of the Thr9–Gly14 (2.4 Å), Gly109–Leu113 (1 Å), and Thr140'–Gly144' (0.8 Å) loop regions upon substrate binding, and these alterations appear to compress the active site for better interactions.

**Analysis of the DTBS–Product Complex at the Active Site.** To study the mechanism of *Mtb* DTBS catalysis, we attempted to capture the ternary complex of the products by soaking the enzyme crystal with DTB, ADP, and  $Mg^{2+}$ . The 2.3 Å electron density map of *Mtb* DTBS clearly reveals the position of the product DTB just opposite the P-loop in the active site. As with DAPA, the C1-carboxyl group of DTB buried inside the pocket forms a hydrogen bond with the main-chain amide nitrogen atoms of Leu146' (2.8 Å), Asn147' (2.6 Å), and Asn182' via a water molecule. This water molecule also causes a peptide flip at Gly111 such that the main-chain oxygen of the residue forms a hydrogen bond with Thr7-OG1. The aliphatic chain of DTB spans the two subunits, making hydrophobic contacts with Pro74, Ala73, Gly111, and Val115. The N7 atom of the ureido ring of DTB is hydrogen bonded to the Asp47-OD1 of the P-loop (3.3 Å), and the N8 atom is hydrogen bonded to Thr11-OG1 (3.4 Å). This breaks the salt bridge between Arg45 and Asp47 at the active site. Comparison of the DAPA-bound and the DTB- and ADP-bound *Mtb* DTBS structures shows clearly that the substrate and product occupy the same position in the active site. The carboxy end of the tail of the ligand is always involved in anchoring to the other subunit of the dimer, and the diamino end participates in catalysis. The DTB aliphatic chain is in a different confirmation when compared to *E. coli* DTBS because the N1-ureido ring hydrogen bonds with Asp47 rather than Thr41 (18). The *Mtb* DTBS active site is lined by a short loop (Gly42–Asp47) whereas the active site of the *E. coli* enzyme is an extension of two antiparallel  $\beta$ -strands (Gly42–Ser53). There are three continuous Asp residues in this region of the *Mtb* DTBS active site: Asp47, which hydrogen bonds with Arg45 as well as the substrate or product, Asp48, which hydrogen bonds with Arg67 (3.5 and 3.3 Å), and Asp49-OD1, which hydrogen bonds with Lys37-NZ (2.9 Å) or a  $Mg^{2+}$  ion.

It appears that the phosphate ion present in the crystallization condition of the DTB- and ADP-bound *Mtb* DTBS structure outcompetes ADP for the nucleotide-binding site. However, there is one phosphate ion bound at the P-loop that is similar to the  $\beta$ -phosphate of ADP and a second phosphate ion present between the P-loop-bound phosphate and DTB that occupies the  $\gamma$ -phosphate position. This mimics the position of the intermediate DTB– $P_i$ –ADP complex at the active site just prior to product release. The phosphate bound at the P-loop causes all of the main-chain amide nitrogen atoms in this region, Thr11–Lys15, to orient inward and create a positively charged environment for tight binding of the nucleotide phosphate group. The Thr11 side chain also changes its rotamer 90° in response to hydrogen bond formation with the  $\gamma$ -phosphate-O4, with a transition of 1 Å toward the active site. These phosphate ions are kept in position by conserved lysine residues (15 and 37) and the magnesium ion. Analysis of the DTB- and phosphate-bound *Mtb* DTBS structure thus demonstrates that the P-loop is involved in binding both substrates at the enzyme active site, providing a rationale for the unusually long peptide sequence at this region.

DTBS, like other nucleotide-binding proteins, uses divalent metal ions such as  $Mg^{2+}$  for stabilizing the phosphate groups, mostly  $\beta$  and  $\gamma$ , of the nucleotides. The DTB- and ADP-bound *Mtb* DTBS structure displays octahedral coordination of the

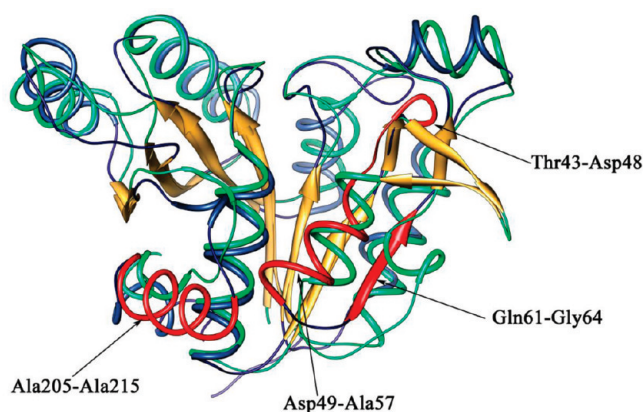


FIGURE 13: Superimposition of  $C_{\alpha}$  atoms of *E. coli* and *Mtb* DTBS monomers. Ribbon diagram of an overlay of *E. coli* DTBS (PDB code: 1BYI) structure (cyan) on *Mtb* DTBS (blue). All core  $\beta$ -strands (gold) from both of the structures overlay very well. The arrows point toward the major differences in the two structures (red). The rmsd for 224  $C_{\alpha}$  atoms for both chains is 1.79 Å.

$Mg^{2+}$  ion between the two oxygen atoms from each of the  $\beta$ - and  $\gamma$ -phosphate groups and the side chains of residues Thr16-OG1, Asp49-OD1, and Glu108-OE1. These residues are conserved in *E. coli* DTBS and nearly conserved in *Helicobacter pylori* DTBS, with Asp49 replaced by Asn46.

**Comparison with Other DTBS Structures.** Superimposition of the *Mtb* and *E. coli* DTBS structures (PDB code: 1BYI, sequence identity 28%) results in an rmsd of approximately 1.79 Å and reveals significant structural differences, justifying the failure of molecular replacement using the *E. coli* DTBS structure as a search model (Figure 13). Interestingly, when the *Mtb* DTBS structure was overlaid with a recently solved DTBS structure from *H. pylori* (PDB code: 2QMO, sequence identity 18%, rmsd = 1.05 Å for 111  $C_{\alpha}$  atoms), similar differences in the overall structure were found. First, there are two extended antiparallel  $\beta$ -strands of unknown function between residues Gly42–Ser53 at the *E. coli* DTBS active site in place of the short loop (Gly42–Asp47) present in *Mtb*. The active site of the *H. pylori* enzyme contains a long loop (Lys35–Ser49) in this region, whereas the *E. coli* and *H. pylori* enzymes have a long loop followed by a short, one-turn helix in residues Arg62–Pro72 (*E. coli*) and Leu61–Ile70 (*H. pylori*), *Mtb* DTBS has a single  $\beta$ -strand ( $\beta$ 3) in the corresponding Gln61–Leu65 region. Third, there is a stretch of three short one-turn helices connected by loops in the *E. coli* DTBS C-terminal region (Pro209–Asn224), with some disordered parts in both the apo and substrate complexed enzymes (PDB codes: 1DTS, 1DAI, 1DAE), while the *Mtb* DTBS has a long helix ( $\alpha$ 9, Ala205–Ala215) followed by a short one-turn helix in the same region. The short stretches of helix at the C-terminus of *E. coli* DTBS might be responsible for its flexibility and subsequent disordered electron density upon solvent exposure. The *H. pylori* DTBS has an entirely different structure at its C-terminus, a short loop with one-turn helix in lieu of the  $\beta$ 7 strand and  $\alpha$ -helices 8 and 9 of the *Mtb* enzyme. Since we have seen that the adenine ring of the nucleotide binds to this region in *Mtb* and *E. coli* DTBS, the exact mode of nucleotide binding in the *H. pylori* DTBS is unclear and awaits elucidation by a nucleotide-bound enzyme structure.

The residues in the P-loop motif are different in all three DTBS proteins: the *Mtb* enzyme has glycine residues and its *E. coli* and *H. pylori* counterparts have charged residues, Glu and Asp, and

Asn, respectively. In *E. coli* DTBS, Lys148 forms a salt bridge with Glu12. Binding of the nucleotide to the Walker motif breaks this bond, and the Glu12 side chain turns toward the  $\beta$ -phosphate of ATP and DAPA-carbamate at the active site. Indeed, Lys148 stabilizes the P-loop by supporting the pocket formed at the back of the loop through its interaction with Glu12. The *Mtb* DTBS has glycine and aspartate residues in place of Glu12 and Lys148 and therefore lacks the ionic interaction found in the active site of the *E. coli* enzyme.

**Possible Mechanism of DTBS Reaction.** Based on the *Mtb* DTBS structures complexed with substrate and products, we can outline a reaction mechanism for this amidoligase. Like *E. coli* DTBS catalysis (68), the *Mtb* enzyme reaction involves three steps: carbamylation of the N7 position of DAPA, formation of a carbamate–phosphoric anhydride intermediate, and, ultimately, closure of the ureido ring to form DTB and release of the inorganic phosphate.

Carbamylation is possible at both the N7 and N8 positions of DAPA in solution (69). The DAPA-bound *Mtb* DTBS structure suggests that this enzyme has specificity for N7-carbamate, but it is not clear whether the carbamylation is catalyzed or whether it happens freely in solution. In the next step of the reaction, one of the carbamate oxygen atoms attacks the  $\gamma$ -phosphate of ATP, evident by the positions of the carbamate-carboxyl group and  $P_i$  in the DAPA- and DTB-complexed structures. Protonation of the linking oxygen atom facilitates cleavage of the bond between the  $\beta$ - and  $\gamma$ -phosphates of ATP. A water molecule (W221 in chain A) in the active site abstracts one of the protons from the adjacent N8 amino group. The Lys37 remains in close enough proximity to the phosphate–carbamate anhydride intermediate to stabilize the complex. Closure of the DTB ureido ring requires a second deprotonation of the N8 atom of the carbamate phosphoric anhydride for attack on the carboxy carbon. Previously, it was thought that Asp47 acted as a base for this proton abstraction. Asp47 is present in the loop region of the active site, a unique feature of this DTBS enzyme. However, kinetic studies show that a D47A mutation does not abolish enzyme activity, suggesting that the residue may not be involved in proton abstraction (data not shown). In the *Mtb* enzyme the lack of a carbamate phosphate anhydride-complexed DTBS prevents unambiguous identification of the residue responsible for proton abstraction. However, based on a structural comparison of carbamate phosphate anhydride complex and native *E. coli* DTBS (19) as well as analogy to the  $p21^{ras}$  protein mechanism (70, 71), the oxygen atom on the phosphate of the intermediate complex may act as a base. A second oxygen atom in the same phosphate group might extract another proton from the N8 atom of the complex after ureido ring closure, thereby neutralizing one of its negative charges, releasing the inorganic phosphate, and forming DTB.

**Implications for DTBS Inhibitors.** The natural antibiotic acidomycin has a chemical structure similar to DTB and biotin and has good whole cell activity against *Mtb* (MIC = 0.0625–0.125  $\mu$ g/mL) (25). However, our studies show that *Mtb* DTBS is not the target of acidomycin as the drug fails to inhibit the DTBS reaction at concentrations up to 200  $\mu$ M. Low yield of the enzyme precluded further kinetic analysis with different compounds. Future candidates for *Mtb* DTBS inhibitors include DAPA carbamate analogues and variable length analogues of DAPA and KAPA. Mimics of the carbamate–phosphoric anhydride complex may also be good inhibitors.

## CONCLUSION

We have determined the crystal structures of two *Mtb* biotin biosynthetic enzymes, 7,8-diaminopelargonic acid synthase (DAPAS) and dethiobiotin synthetase (DTBS). These enzymes are promising drug targets as the biotin biosynthesis pathway is required for *Mtb* survival during infection but absent in humans. Moreover, abolition of biotin production leads to irreversible cell death when *Mtb* is starved for the compound, suggesting that inhibitors of the pathway could be bactericidal.

Beyond their utility as potential drug targets, the *Mtb* DAPAS and DTBS crystal structures yield basic biological insights into their mechanisms of catalysis. The mode by which the DAPAS recognizes dual substrates, the amino donor SAM and acceptor KAPA, was not known despite the availability of the *E. coli* crystal structure. The *Mtb* and *E. coli* DAPAS structures have similar folds and conserved active site residues, making comparison studies feasible. Superimposition of the *Mtb* DAPAS structure bound to the SAM analogue sinefungin on the KAPA-complexed *E. coli* enzyme indicates that the mechanism of substrate recognition for this enzyme is different than other aminotransferases. Both *Mtb* and *E. coli* DAPAS have an active site tyrosine that is critical for substrate interaction. Interestingly, the DAPAS of certain *Bacillus* species lack this residue. We solved the apo and KAPA-bound *B. subtilis* DAPAS structures to show that there is an alternate KAPA binding pattern in the absence of the tyrosine. The *B. subtilis*, *E. coli*, and *Mtb* DAPAS structures also reveal the importance of the hydrogen bond network Tyr25–Tyr157–Asp160 for maintenance of the active site structure.

The overall fold of *Mtb* DTBS differs from other organisms. On the basis of our substrate- and product-bound DTBS structures, we identified key components required for catalysis, some of which are not conserved in *E. coli*, and from these derived an enzyme mechanism.

Finally, we have found that the active site of *Mtb* DTBS is more solvent exposed than *Mtb* DAPAS, which has a tunneled active site. Our characterization of the *Mtb* DAPAS and DTBS active sites and of the mechanism by which they bind substrates and products is a starting point in the design of new inhibitors against these enzymes and, by extension, a metabolic pathway that is critical for *Mtb* survival.

## ACKNOWLEDGMENT

The authors thank Tracey Musa and Siaska Castro for assistance on the manuscript and Dr. Kimberly D. Grimes for the preparation of acidomycin.

## REFERENCES

- Moss, J., and Lane, M. D. (1971) The biotin-dependent enzymes. *Adv. Enzymol. Relat. Areas Mol. Biol.* 35, 321–442.
- Gomez, J. E., and McKinney, J. D. (2004) *M. tuberculosis* persistence, latency, and drug tolerance. *Tuberculosis (Edinburgh)* 84, 29–44.
- Keer, J., Smeulders, M. J., Gray, K. M., and Williams, H. D. (2000) Mutants of *Mycobacterium smegmatis* impaired in stationary-phase survival. *Microbiology* 146 (Part 9), 2209–2217.
- Betts, J. C., Lukey, P. T., Robb, L. C., McAdam, R. A., and Duncan, K. (2002) Evaluation of a nutrient starvation model of *Mycobacterium tuberculosis* persistence by gene and protein expression profiling. *Mol. Microbiol.* 43, 717–731.
- Sasseti, C. M., and Rubin, E. J. (2003) Genetic requirements for mycobacterial survival during infection. *Proc. Natl. Acad. Sci. U.S.A.* 100, 12989–12994.
- Chiang, S. L., and Mekalanos, J. J. (1998) Use of signature-tagged transposon mutagenesis to identify *Vibrio cholerae* genes critical for colonization. *Mol. Microbiol.* 27, 797–805.
- Cole, S. T., Brosch, R., Parkhill, J., Garnier, T., Churcher, C., Harris, D., Gordon, S. V., Eiglmeier, K., Gas, S., Barry, C. E., 3rd, Tekaia, F., Badcock, K., Basham, D., Brown, D., Chillingworth, T., Connor, R., Davies, R., Devlin, K., Feltwell, T., Gentles, S., Hamlin, N., Holroyd, S., Hornsby, T., Jagels, K., Krogh, A., McLean, J., Moule, S., Murphy, L., Oliver, K., Osborne, J., Quail, M. A., Rajandream, M. A., Rogers, J., Rutter, S., Seeger, K., Skelton, J., Squares, R., Squares, S., Sulston, J. E., Taylor, K., Whitehead, S., and Barrell, B. G. (1998) Deciphering the biology of *Mycobacterium tuberculosis* from the complete genome sequence. *Nature* 393, 537–544.
- Izumi, Y., Kano, Y., Inagaski, K., and Yamada, H. (1981) Characterisation of biotin biosynthetic enzymes of *Bacillus sphaericus*: a dethiobiotin producing bacterium. *Agric. Biol. Chem.* 45, 1983–1989.
- Van Arsdell, S. W., Perkins, J. B., Yocum, R. R., Luan, L., Howitt, C. L., Chatterjee, N. P., and Pero, J. G. (2005) Removing a bottleneck in the *Bacillus subtilis* biotin pathway: bioA utilizes lysine rather than S-adenosylmethionine as the amino donor in the KAPA-to-DAPA reaction. *Biotechnol. Bioeng.* 91, 75–83.
- Phalip, V., Kuhn, I., Lemoine, Y., and Jeltsch, J. M. (1999) Characterization of the biotin biosynthesis pathway in *Saccharomyces cerevisiae* and evidence for a cluster containing BIO5, a novel gene involved in vitamer uptake. *Gene* 232, 43–51.
- Pinon, V., Ravel, S., Douce, R., and Alban, C. (2005) Biotin synthesis in plants. The first committed step of the pathway is catalyzed by a cytosolic 7-keto-8-aminopelargonic acid synthase. *Plant Physiol.* 139, 1666–1676.
- Stoner, G. L., and Eisenberg, M. A. (1975) Purification and properties of 7,8-diaminopelargonic acid aminotransferase. *J. Biol. Chem.* 250, 4029–4036.
- Sandmark, J., Eliot, A. C., Famm, K., Schneider, G., and Kirsch, J. F. (2004) Conserved and nonconserved residues in the substrate binding site of 7,8-diaminopelargonic acid synthase from *Escherichia coli* are essential for catalysis. *Biochemistry* 43, 1213–1222.
- Eliot, A. C., Sandmark, J., Schneider, G., and Kirsch, J. F. (2002) The dual-specific active site of 7,8-diaminopelargonic acid synthase and the effect of the R391A mutation. *Biochemistry* 41, 12582–12589.
- Kack, H., Sandmark, J., Gibson, K., Schneider, G., and Lindqvist, Y. (1999) Crystal structure of diaminopelargonic acid synthase: evolutionary relationships between pyridoxal-5'-phosphate-dependent enzymes. *J. Mol. Biol.* 291, 857–876.
- Sandmark, J., Mann, S., Marquet, A., and Schneider, G. (2002) Structural basis for the inhibition of the biosynthesis of biotin by the antibiotic ampicillin. *J. Biol. Chem.* 277, 43352–43358.
- Huang, W., Lindqvist, Y., Schneider, G., Gibson, K. J., Flint, D., and Lorimer, G. (1994) Crystal structure of an ATP-dependent carboxylase, dethiobiotin synthetase, at 1.65 Å resolution. *Structure* 2, 407–414.
- Kack, H., Sandmark, J., Gibson, K. J., Schneider, G., and Lindqvist, Y. (1998) Crystal structure of two quaternary complexes of dethiobiotin synthetase, enzyme-MgADP-AlF<sub>3</sub>-diaminopelargonic acid and enzyme-MgADP-dethiobiotin-phosphate; implications for catalysis. *Protein Sci.* 7, 2560–2566.
- Kack, H., Gibson, K. J., Lindqvist, Y., and Schneider, G. (1998) Snapshot of a phosphorylated substrate intermediate by kinetic crystallography. *Proc. Natl. Acad. Sci. U.S.A.* 95, 5495–5500.
- Alexeev, D., Baxter, R. L., Smekal, O., and Sawyer, L. (1995) Substrate binding and carboxylation by dethiobiotin synthetase—a kinetic and X-ray study. *Structure* 3, 1207–1215.
- Ashkenazi, T., Widberg, A., Nudelman, A., Wittenbach, V., and Flint, D. (2005) Inhibitors of biotin biosynthesis as potential herbicides: part 2. *Pest Manag. Sci.* 61, 1024–1033.
- Ashkenazi, T., Pinkert, D., Nudelman, A., Widberg, A., Wexler, B., Wittenbach, V., Flint, D., and Nudelman, A. (2007) Aryl chain analogues of the biotin vitamers as potential herbicides. Part 3. *Pest Manag. Sci.* 63, 974–1001.
- Rendina, A. R., Taylor, W. S., Gibson, K., Lorimer, G., Rayner, D., Lockett, B., Kranis, K., Wexler, B., Marcovici-Mizrahi, D., Nudelman, A., Nudelman, A., Marsili, E., Chi, H., Wawrzak, Z., Calabrese, J., Huang, W., Jia, J., Schneider, G., Lindqvist, Y., and Yang, G. (1999) The design and synthesis of inhibitors of dethiobiotin synthetase as potential herbicides. *Pestic. Sci.* 55, 236–247.
- Okami, Y., Kitahara, T., Hamada, M., Naganawa, H., and Kondo, S. (1974) Studies on a new amino acid antibiotic, ampicillin. *J. Antibiot. (Tokyo)* 27, 656–664.
- Grundy, W. E., Whitman, A. O., Rdzok, E. G., Hanes, M. E., and Sylvester, J. C. (1952) Actithiazic acid. I. Microbiological studies. *Antibiot. Chemother.* 11, 399–408.
- Kitahara, T., Hotta, K., Yoshida, M., and Okami, Y. (1975) Biological studies of ampicillin. *J. Antibiot. (Tokyo)* 28, 215–221.
- Hwang, K. (1952) Actithiazic acid: pharmacological studies. *Antibiot. Chemother.* 11, 453–459.

28. Mann, S., and Ploux, O. (2006) 7,8-Diaminopelargonic acid aminotransferase from *Mycobacterium tuberculosis*, a potential therapeutic target. Characterization and inhibition studies. *FEBS J.* 273, 4778–4789.
29. Cleland, W. W. (1979) Optimizing coupled enzyme assays. *Anal. Biochem.* 99, 142–145.
30. Mach, H., Middaugh, C. R., and Lewis, R. V. (1992) Statistical determination of the average values of the extinction coefficients of tryptophan and tyrosine in native proteins. *Anal. Biochem.* 200, 74–80.
31. Sandalova, T., Schneider, G., Kack, H., and Lindqvist, Y. (1999) Structure of dethiobiotin synthetase at 0.97 Å resolution. *Acta Crystallogr., Sect. D: Biol. Crystallogr.* 55, 610–624.
32. Otwinowski, Z., and Minor, W. (1997) *Methods Enzymol.* 276, 307–326.
33. Pflugrath, J. W. (1999) The finer things in X-ray diffraction data collection. *Acta Crystallogr., Sect. D: Biol. Crystallogr.* 55, 1718–1725.
34. Leslie, A. G. W. (1992) in Jt. CCP4/ESF-EAMCB Newslett. Protein Crystallogr.
35. Evans, P. R. (1993) Data Collection and Processing, Daresbury Laboratory, Warrington, U.K.
36. Storoni, L. C., McCoy, A. J., and Read, R. J. (2004) Likelihood-enhanced fast rotation functions. *Acta Crystallogr.* 60, 432–438.
37. Schneider, T.R., and Sheldrick, G.M. (2002) Substructure solution with SHELXD. *Acta Crystallogr. D* 58, 1772–1779.
38. Cowtan, K. D., and Main, P. (1996) Phase combination and cross validation in iterated density-modification calculations. *Acta Crystallogr.* 52, 43–48.
39. McRee, D. E. (1999) XtalView/Xfit—a versatile program for manipulating atomic coordinates and electron density. *J. Struct. Biol.* 125, 156–165.
40. Emsley, P., and Cowtan, K. (2004) Coot: model-building tools for molecular graphics. *Acta Crystallogr.* 60, 2126–2132.
41. Reddy, V., Swanson, S. M., Segelke, B., Kantardjieff, K. A., Sacchettini, J. C., and Rupp, B. (2003) Effective electron-density map improvement and structure validation on a Linux multi-CPU web cluster: The TB Structural Genomics Consortium Bias Removal Web Service. *Acta Crystallogr. D Biol. Crystallogr.* 59, 2200–2210.
42. Brunger, A. T., Adams, P. D., Clore, G. M., DeLano, W. L., Gros, P., Grosse-Kunstleve, R. W., Jiang, J. S., Kuszewski, J., Nilges, M., Pannu, N. S., Read, R. J., Rice, L. M., Simonson, T., and Warren, G. L. (1998) Crystallography & NMR system: a new software suite for macromolecular structure determination. *Acta Crystallogr.* 54, 905–921.
43. Laskowski, R. A., MacArthur, M. W., Moss, D. S., and Thornton, J. M. (1993) *J. Appl. Crystallogr.* 26, 283–291.
44. Parish, T. (2003) Starvation survival response of *Mycobacterium tuberculosis*. *J. Bacteriol.* 185, 6702–6706.
45. Hondalus, M. K., Bardarov, S., Russell, R., Chan, J., Jacobs, W. R., Jr., and Bloom, B. R. (2000) Attenuation of and protection induced by a leucine auxotroph of *Mycobacterium tuberculosis*. *Infect. Immun.* 68, 2888–2898.
46. Pavelka, M. S., Jr., and Jacobs, W. R., Jr. (1996) Biosynthesis of diaminopimelate, the precursor of lysine and a component of peptidoglycan, is an essential function of *Mycobacterium smegmatis*. *J. Bacteriol.* 178, 6496–6507.
47. Han, Q., and Li, J. (2004) pH dependence, substrate specificity and inhibition of human kynurenine aminotransferase I. *Eur. J. Biochem.* 271, 4804–4814.
48. Goto, M., Omi, R., Miyahara, I., Hosono, A., Mizuguchi, H., Hayashi, H., Kagamiyama, H., and Hirotsu, K. (2004) Crystal structures of glutamine:phenylpyruvate aminotransferase from *Thermus thermophilus* HB8: induced fit and substrate recognition. *J. Biol. Chem.* 279, 16518–16525.
49. Bhor, V. M., Dev, S., Vasanthakumar, G. R., and Surolia, A. (2006) Spectral and kinetic characterization of 7,8-diaminopelargonic acid synthase from *Mycobacterium tuberculosis*. *IUBMB Life* 58, 225–233.
50. Breen, R. S., Campopiano, D. J., Webster, S., Brunton, M., Watt, R., and Baxter, R. L. (2003) The mechanism of 7,8-diaminopelargonate synthase; the role of S-adenosylmethionine as the amino donor. *Org. Biomol. Chem.* 1, 3498–3499.
51. Stoner, G. L., and Eisenberg, M. A. (1975) Biosynthesis of 7,8-diaminopelargonic acid from 7-keto-8-aminopelargonic acid and S-adenosyl-L-methionine. The kinetics of the reaction. *J. Biol. Chem.* 250, 4037–4043.
52. Eisenberg, M. A., and Krell, K. (1979) Dethiobiotin synthetase. *Methods Enzymol.* 62, 348–352.
53. Jager, J., Moser, M., Sauder, U., and Jansonius, J. N. (1994) Crystal structures of *Escherichia coli* aspartate aminotransferase in two conformations. Comparison of an unliganded open and two liganded closed forms. *J. Mol. Biol.* 239, 285–305.
54. Hohenester, E., and Jansonius, J. N. (1994) Crystalline mitochondrial aspartate aminotransferase exists in only two conformations. *J. Mol. Biol.* 236, 963–968.
55. Capitani, G., Eliot, A. C., Gut, H., Khomutov, R. M., Kirsch, J. F., and Grutter, M. G. (2003) Structure of L-aminocyclopropane-1-carboxylate synthase in complex with an amino-oxy analogue of the substrate: implications for substrate binding. *Biochim. Biophys. Acta* 1647, 55–60.
56. Toney, M. D., Pascarella, S., and De Biase, D. (1995) Active site model for gamma-aminobutyrate aminotransferase explains substrate specificity and inhibitor reactivities. *Protein Sci.* 4, 2366–2374.
57. Hirotsu, K., Goto, M., Okamoto, A., and Miyahara, I. (2005) Dual substrate recognition of aminotransferases. *Chem. Rec.* 5, 160–172.
58. Koshland, D. E. (1958) Application of a theory of enzyme specificity to protein synthesis. *Proc. Natl. Acad. Sci. U.S.A.* 44, 98–104.
59. Koshland, D. E. (1994) The key-lock theory and the induced fit theory. *Angew. Chem., Int. Ed. Engl.* 33, 2375–2378.
60. Fischer, E. (1894) Einfluss der configuration auf die wirkung der enzyme. *Ber. Deut. Chem. Ges.* 27, 2985–2993.
61. Mani Tripathi, S., and Ramachandran, R. (2006) Direct evidence for a glutamate switch necessary for substrate recognition: crystal structures of lysine epsilon-aminotransferase (Rv3290c) from *Mycobacterium tuberculosis* H37Rv. *J. Mol. Biol.* 362, 877–886.
62. Fenn, T. D., Stamper, G. F., Morollo, A. A., and Ringe, D. (2003) A side reaction of alanine racemase: transamination of cycloserine. *Biochemistry* 42, 5775–5783.
63. Shah, S. A., Shen, B. W., and Brunger, A. T. (1997) Human ornithine aminotransferase complexed with L-canaline and gabaculine: structural basis for substrate recognition. *Structure* 5, 1067–1075.
64. Hennig, M., Grimm, B., Contestabile, R., John, R. A., and Jansonius, J. N. (1997) Crystal structure of glutamate-L-semialdehyde aminomutase: an alpha2-dimeric vitamin B6-dependent enzyme with asymmetry in structure and active site reactivity. *Proc. Natl. Acad. Sci. U.S.A.* 94, 4866–4871.
65. Storic, P., De Biase, D., Bossa, F., Bruno, S., Mozzarelli, A., Peneff, C., Silverman, R. B., and Schirmer, T. (2004) Structures of gamma-aminobutyric acid (GABA) aminotransferase, a pyridoxal 5'-phosphate, and [2Fe-2S] cluster-containing enzyme, complexed with gamma-ethynyl-GABA and with the antiepilepsy drug vigabatrin. *J. Biol. Chem.* 279, 363–373.
66. Pai, E. F., Kregel, U., Petsko, G. A., Goody, R. S., Kabsch, W., and Wittinghofer, A. (1990) Refined crystal structure of the triphosphate conformation of H-ras p21 at 1.35 Å resolution: implications for the mechanism of GTP hydrolysis. *EMBO J.* 9, 2351–2359.
67. Silva, M. M., Poland, B. W., Hoffman, C. R., Fromm, H. J., and Honzatko, R. B. (1995) Refined crystal structures of unligated adenylosuccinate synthetase from *Escherichia coli*. *J. Mol. Biol.* 254, 431–446.
68. Yang, G., Sandalova, T., Lohman, K., Lindqvist, Y., and Rendina, A. R. (1997) Active site mutants of *Escherichia coli* dethiobiotin synthetase: effects of mutations on enzyme catalytic and structural properties. *Biochemistry* 36, 4751–4760.
69. Gibson, K. J., Lorimer, G. H., Rendina, A. R., Taylor, W. S., Cohen, G., Gatenby, A. A., Payne, W. G., Roe, D. C., Lockett, B. A., and Nudelman, A.; et al. (1995) Dethiobiotin synthetase: the carbonylation of 7,8-diaminonanoic acid proceeds regiospecifically via the N7-carbamate. *Biochemistry* 34, 10976–10984.
70. Schweins, T., Geyer, M., Scheffzek, K., Warshel, A., Kalbitzer, H. R., and Wittinghofer, A. (1995) Substrate-assisted catalysis as a mechanism for GTP hydrolysis of p21ras and other GTP-binding proteins. *Nat. Struct. Biol.* 2, 36–44.
71. Schweins, T., Geyer, M., Kalbitzer, H. R., Wittinghofer, A., and Warshel, A. (1996) Linear free energy relationships in the intrinsic and GTPase activating protein-stimulated guanosine 5'-triphosphate hydrolysis of p21ras. *Biochemistry* 35, 14225–14231.
72. Wallace, A. C., Laskowski, R. A., and Thornton, J. M. (1995) LIGPLOT: a program to generate schematic diagrams of protein-ligand interactions. *Protein Eng.* 8, 127–134.